Nonclinical pharmacokinetics and biodistribution of VSV-GP using methods to decouple input drug disposition and viral replication

Richard Dambra,[1,4,6] Andrea Matter,[2,6] Kaitlynn Graca,[1] Saeed Salehin Akhand,[1] Saurin Mehta,[2] Ashlee Bell-Cohn,[1] Joyce M. Swenson,[1] Sadia Abid,[3] Dongyue Xin,[3] Cedric Lewis,[2] Luke Coyle,[2] Min Wang,[2] Kathleen Bunosso,[2] Michelle Maugiri,[2] Richard Ruiz,[2] Corey M. Cirillo,[2] Birgit Fogal,[2] Christine Grimaldi,[1,5] Adam Vigil,[1] Charles Wood,[2] and Joseph Ashour[1]

[1]Drug Metabolism and Pharmacokinetics, Boehringer Ingelheim Pharmaceuticals, Inc., Ridgefield, CT 06877, USA; [2]Nonclinical Drug Safety, Boehringer Ingelheim Pharmaceuticals, Inc., Ridgefield, CT 06877, USA; [3]Material and Analytical Sciences, Boehringer Ingelheim Pharmaceuticals, Inc., Ridgefield, CT 06877, USA; [4]Drexel University School of Biomedical Engineering, Science and Health Systems, Philadelphia, PA 19104, USA

Viral replication places oncolytic viruses (OVs) in a unique niche in the field of drug pharmacokinetics (PK) as their self-amplification obscures exposure-response relationships. Moreover, standard bioanalytical techniques are unable to distinguish the input from replicated drug products. Here, we combine two novel approaches to characterize PK and biodistribution (BD) after systemic administration of vesicular stomatitis virus pseudotyped with lymphocytic choriomeningitis virus glycoprotein (VSV-GP) in healthy mice. First: to decouple input drug PK/BD versus replication PK/BD, we developed and fully characterized a replication-incompetent tool virus that retained all other critical attributes of the drug. We used this approach to quantify replication in blood and tissues and to determine its impact on PK and BD. Second: to discriminate the genomic and antigenomic viral RNA strands contributing to replication dynamics in tissues, we developed an *in situ* hybridization method using strand-specific probes and assessed their spatiotemporal distribution in tissues. This latter approach demonstrated that distribution, transcription, and replication localized to tissue-resident macrophages, indicating their role in PK and BD. Ultimately, our study results in a refined PK/BD profile for a replicating OV, new proposed PK parameters, and deeper understanding of OV PK/BD using unique approaches that could be applied to other replicating vectors.

INTRODUCTION

Replication-competent oncolytic viruses (OVs) are emerging and promising cancer immunotherapies with demonstrable clinical efficacy.[1–4] Their pharmacological effects (e.g., oncolysis, progeny infection, local inflammation, immune activation, and *in situ* cargo expression) are mediated largely by viral replication in the tumor, which drives the drug's potency.[5–7] Rhabdoviruses are excellent OV candidates owing to their rapid cytopathic replication, low seroprevalence in humans, immunomodulatory capacity, and ease of achieving high titers in production cell lines.[8–12] The prototypical rhabdovirus vesicular stomatitis virus (VSV) has demonstrated therapeutic efficacy in a variety of mouse cancer models,[8,13–16] as well as early clinical proof of principle and tolerability in canine cancer patient trials and phase I/II human cancer patient trials.[17–19]

Comprehensive pharmacokinetic (PK) and pharmacodynamic (PD) characterization is essential for cancer drug development. PK is the study of *drug fate* in the body and is conducted by measuring drug (and metabolite) concentrations over time—typically in blood or serum. Concentration-time profiles are then used to calculate PK parameters. The primary PK parameters, clearance (CL) and volume of distribution (V_d), are used to describe the disposition and elimination of drugs, which enables their half-life ($t_{1/2}$) calculation. Area under concentration-time curve (AUC) and maximal concentration (C_{max}) are used to quantify exposure. Biodistribution (BD) studies may also be performed as part of the PK assessment to determine distribution of the dosed therapeutic throughout tissues in the body (particularly relevant for viral vectors as a critical endpoint in preclinical safety and pharmacology studies).[20,21] In contrast to PK, PD is the study of *drug effect* and is conducted by measuring the patient response to drug, as defined by one or more biomarkers that are selected based on the drug's specific mechanism of action. Characterizing the relationship between PK and PD helps determine clinical strategies for therapeutic development (e.g., human efficacious dose predictions and defining optimal dosing regimens).

In general, the fate of systemically administered viral vector-based drugs is known—they rapidly clear from the blood within minutes to hours and distribute to tissues throughout the body, particularly the liver and lymphoid organs.[22–30] Distribution is driven primarily by interactions between the virus and the mononuclear phagocytic system (MPS) via a panoply of nonspecific interactions (e.g., sialic acids) and serum factors (e.g., complement and natural antibodies).[15,24,31–34] To date, PK/BD studies of OVs have used various methods for measuring virus replication *in vivo* (e.g., qRT-PCR, infectivity assays, protein reporters, reporter imaging[35–41]), which do not easily discern between the input virus disposition and replication. Furthermore, replication impacts both concentration-time (PK/BD) and concentration-effect (PD) profiles, resulting in a bidirectional relationship between PK and PD, which has been alluded to by others.[6,35,42,43] Thus, standard PK analysis and dose prediction approaches commonly used for other drug modalities (e.g., biologics and small molecules) are not easily applied to replication-competent OVs.[44] Indeed, unlike traditional biologics or small molecules, it is not common to describe the fate of replication-competent OVs using traditional PK parameters, likely because replication confounds PK parameter calculations (e.g., CL rates or $t_{1/2}$ values in the context of increasing drug levels).[45]

Herein, we characterize the PK and BD of a model OV, VSV pseudotyped with the lymphocytic choriomeningitis virus (LCMV) glycoprotein (VSV-GP). VSV-GP, and variants thereof, are currently undergoing preclinical and clinical development for treatment of solid tumors.[46–48] For this characterization, we developed a UV light-inactivated tool virus (VSV-GP^{UV}) that could be used to decouple input drug concentrations from replicated drug concentrations *in vivo* (a.k.a. input and replicated virus). Our approach resulted in two unique PK profiles: PK^1 to describe the concentration-time profile of *input* virus and PK^2 to describe the concentration-time profile of *replicated* virus products. Importantly, this approach facilitated calculation of classical PK parameters to quantify input disposition as well as additional unique PK parameters (ΔAUC and AUC$_R$) that enabled quantification of replication in blood and tissues. In addition, by employing a unique strand-specific *in situ* hybridization (ISH) method in duplex with immunohistochemistry (IHC), we demonstrate that the PK^1 and PK^2 profiles of VSV-GP in tissue are driven by tissue-resident macrophages. We anticipate these findings will have implications for development of other OVs and replication-competent vectors.

RESULTS
Generation and characterization of VSV-GP^{UV} replication-incompetent tool virus

Toward our goal of a more refined pharmacological assessment of VSV-GP, we set out to uncouple input virus concentrations (PK^1) from replicated virus concentrations (PK^2). As a first step, we used UV irradiation to generate a tool virus that would be nearly identical to VSV-GP, except deficient in its ability to replicate. Early experiments revealed that, despite effective inactivation, UV exposure impacted genome recovery by qRT-PCR (Figure S1). After method optimizations to dampen UV intensity, increasing UV exposures

were then tested to determine a dynamic range of inactivation. As shown in Figure 1A, inactivation was found to be dose-dependent and impacts were observed with exposure times as short as 1 s. By 120 s (equivalent to ~650 mJ/cm^2) of exposure, measured infectious units fell below the limit of detection (LOD) of the assay (~125 tissue culture infectious dose 50% (TCID$_{50}$)/mL). Importantly, these exposure times had minimal to no impact on genome recovery. We confirmed, using light microscopy, a lack of cytopathic effect (CPE) in cells treated with VSV-GP exposed to 60 s (~360 mJ/cm^2) UV irradiation (Figure 1B). Finally, we performed 60 s exposure on VSV-GP expressing GFP (VSV-GP-GFP) to detect whether transgene expression remained despite loss of infectivity. As shown in Figure 1C, GFP expression was not detected in cells infected with VSV-GP-GFP exposed to 60 s UV irradiation.

Next, we further assessed the impacts of UV exposure on specific steps of the VSV-GP life cycle (i.e., cell binding/entry, gene transcription, and progeny release). To examine cell binding/entry, we co-incubated cells with virus and measured the loss of genomes in supernatant over time (as an indirect measure for virus entry). We observed no impact of UV irradiation (up to 60 s) on cell binding/entry (Figure 1D). To examine intracellular transcription, we co-incubated cells with virus and then measured VSV-N RNA in cells over time. As shown in Figure 1E, the impacts of UV irradiation on gene expression were exposure dependent, with near complete loss of transcription observed following 60 s exposure. At the same time points, we measured virus genomes in the supernatants and found that progeny release was also exposure-dependent, with near complete loss of progeny virus following 20 s exposure (Figure 1F). Interestingly, trace residual intracellular VSV-N transcription was detected after exposure of 20 and 60 s (Figure 1E), despite the absence of either released progeny (Figure 1F) or replicated genomic RNA at 6 h (Figure S1). This latter observation is consistent with previous findings that higher UV doses are needed to completely deplete VSV transcription versus infectivity.[49,50]

Having demonstrated the impacts of UV on the VSV-GP life cycle, we next wanted to characterize its impact on VSV-GP antigenic, structural, and morphological integrity. As UV has been demonstrated to crosslink both nucleic acids and proteins,[51–53] we probed for damage to the viral GP using binding immunoassays. As shown in Figures 2A and 2B, UV exposure up to 600 s (~4000 mJ/cm^2) did not impact the ability of VSV-GP to bind either its receptor, α-dystroglycan (αDG),[54,55] or a neutralizing antibody, Wen1.3,[56,57] indicating that the conformational integrity of GP is maintained. As heat-inactivation of virus is known to damage viral protein conformation,[58] we used it as a control for comparison and observed a significant loss in antibody binding potency compared with VSV-GP and VSV-GP^{UV}. Next, we assessed the impacts of UV on virus particle size distribution and particle concentration using nanoparticle tracking analysis (NTA). As shown in Figure 2C, 600 s exposure did not alter particle size distribution or concentration. We further probed for morphological impacts using cryogenic electron microscopy. We found that 60 s of UV exposure did not impart morphological alterations or generate aggregates (Figures 2D and S2).
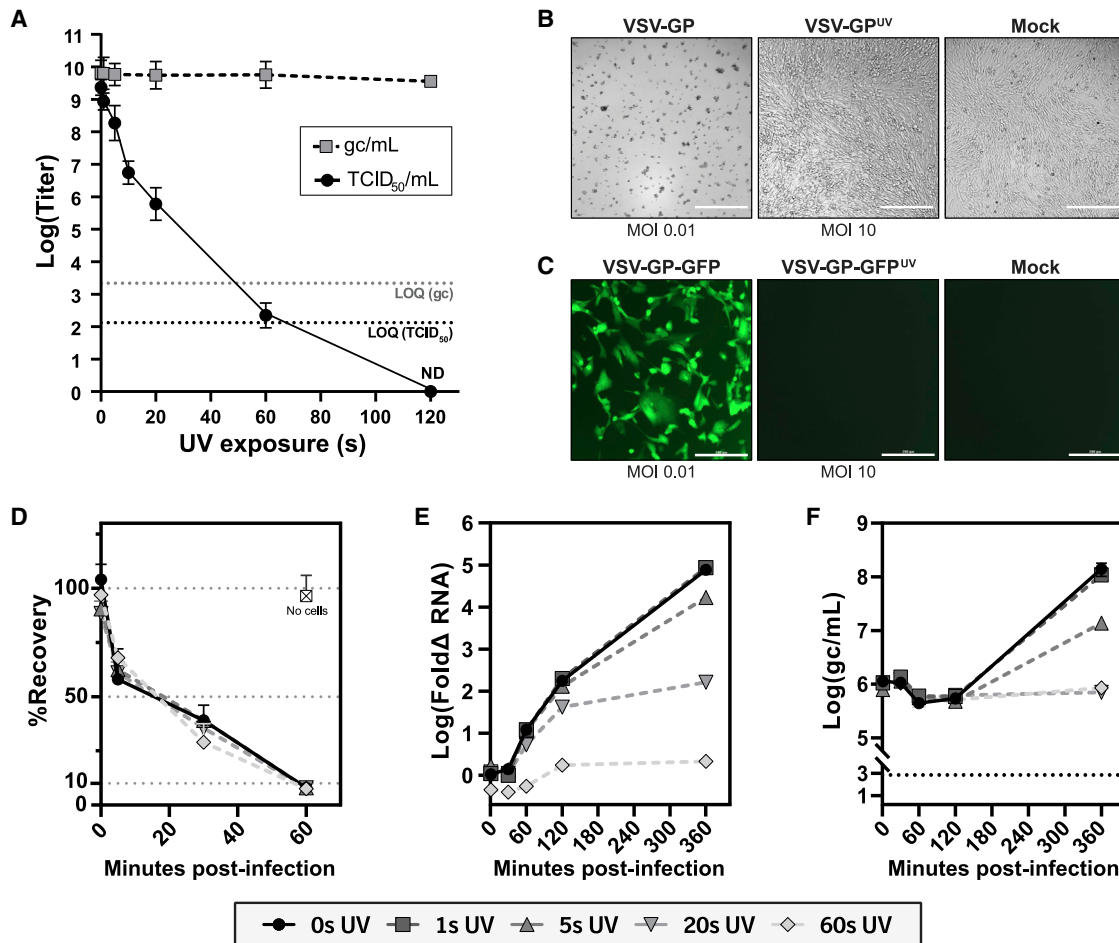
Figure 1. Generation and biological characterization of UV-inactivated tool virus

(A) Viral titers measured in genome copies (gc)/mL and infectious units (TCID$_{50}$/mL) after escalating exposure of UV$_{254}$ irradiation. The geometric means (± geometric SD) of two independent experiments in technical triplicates are plotted. (B) Representative phase-contrast microscopy images of BHK-21 cells 72 h post-virus challenge with VSV-GP (left), VSV-GP^{UV} after 60 s of UV exposure (middle), or mock treated (right). Scale bars, 1 µm. (C) Representative fluorescence microscopy images of BHK-21 cells 16 h post-treatment with VSV-GP-GFP (left), VSV-GP-GFP^{UV} after 6 0s UV exposure (middle), or mock treated (right). Scale bars, 0.2 µm. (D) Viral genomes remaining in supernatant after co-incubation of HEK293-F suspension cells with VSV-GP exposed, or not, to varying levels of UV exposure. The percent recovery (compared with nominal input genomes) is plotted against time through 1 h. (E) Intracellular VSV-N RNA expression in HEK293-F cells over time after adherent synchronized infection. Fold change in relative N expression (in relation to time zero) is plotted over time. Data points represent means (±SD) of biological duplicates (error bars may not be shown if smaller than data point shapes). (F) Viral genomes released from HEK293-F cells measured in supernatants via qRT-PCR. Mean (±SD) genome copies per mL are plotted against time from biological duplicates each in qPCR triplicate. All cell-based assay data is representative of at least three independent experiments. ND, not detected; VSV-N, gene encoding vesicular stomatitis virus nucleoprotein; gc/mL, genome copies per mL; TCID$_{50}$, tissue culture infectious dose 50%.

Early innate responses to virus *in vivo* are expected to influence PK and BD of the input virus, as viral entry is known to induce type-I interferon (IFN) production via input-dependent pathways in addition to pathways dependent on replication.[59,60] To determine whether UV exposure impacted the ability of VSV-GP to induce early IFN in response to input virus, we infected primary mouse splenocytes *ex vivo* with VSV-GP before or after 60 s UV exposure and measured IFN release in supernatants. As shown in Figures 2E and S3, 60 s of UV exposure did not impact the ability of VSV-GP to induce IFN. The IFN released was likely due to input genomes of each test article, as minimal to no replication was observed in the *ex vivo* cultures (Figure S3).

In summary, 60 s UV exposure was sufficient to arrest viral replication and ablate infectious titer while retaining genome recovery, binding, structural, and innate immunogenic properties of live VSV-GP. Based on these results, this exposure level was selected to generate the tool virus (a.k.a. VSV-GP^{UV}) for *in vivo* PK and BD assessment.

Whole-blood PK of VSV-GP and VSV-GP^{UV}

Next, using the tool virus above (60 s exposure), we set out to characterize PK[1] and PK[2] for VSV-GP. For this characterization, BALB/c mice were administered a single intravenous (i.v.) bolus dose of either live VSV-GP or VSV-GP^{UV} at an equivalent genome copy dose
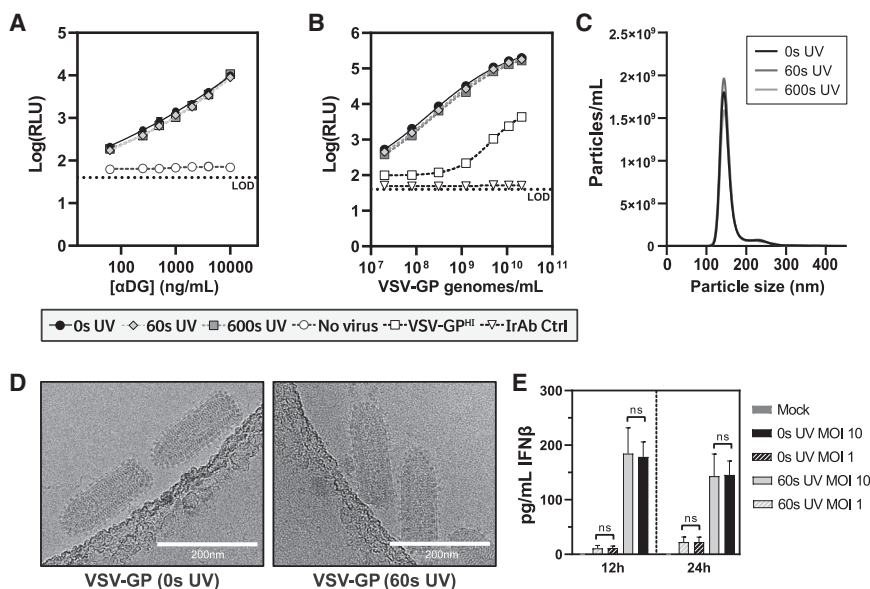
Figure 2. Structural and conformational characterization of UV-inactivated tool virus

(A and B) Binding electrochemiluminescence immuno-assays to measure αDG (A) or an anti-LCMV-GP neutralizing antibody (B) to VSV-GP samples to determine integrity of GP binding. Viruses were coated on plates and then incubated with either increasing amounts of αDG and detected with an anti-αDG detection antibody (A), or anti-LCMV-GP mouse monoclonal antibody and detected with an anti-mouse detection antibody (B). Binding profiles are representative of two independent experiments and data points are mean RLUs of duplicates (±SD), which were curve-fitted with four-parameter nonlinear regression. (C) Particle size distribution profile of VSV-GP before and after 10 min (∼7,400 mJ/cm^2) of UV exposure measured by NTA. (D) Representative cryogenic electron micrographs taken at 73,000× magnification of VSV-GP before (left) and after (right) UV exposure of 60 s (600 s exposure and lower magnification images can be seen in Figure S2). Scale bar, 200 μm. (E) IFN-β release from primary naive BALB/c mouse splenocytes after *ex vivo* treatment with live VSV-GP or VSV-GP^{UV}, where MOI was calculated using input genome copies. At 12 and 24 h post-infection, cell supernatants were collected and measured for IFN-β (and IFN-α, see Figure S3) using an MSD U-plex kit. Bars represent mean concentrations in pg/mL (±SD) from four independent experiments (each performed with n = 2 mice). Statistical testing was performed using ANOVA with Tukey's multiple comparisons test (α = 0.05). αDG, alpha-dystroglycan; RLU, relative light units; LCMV-GP, lymphocytic choriomeningitis virus glycoprotein; mAb, monoclonal antibody; VSV-GP^{HI}, heat-inactivated VSV-GP (65°C for 10 min); IrAb Ctrl, irrelevant antibody control (VSV-GP samples with irrelevant isotype-matched control antibody); IFN, type-I interferon; MSD, MesoScale Discovery; MOI, multiplicity of infection; SD, standard deviation; ns, not significant.

(∼2 × 10^{10} genome copies). Mice dosed with VSV-GP received 10^9 TCID$_{50}$, whereas mice dosed with VSV-GP^{UV} received <10^2 TCID$_{50}$. Whole-blood samples were collected at 12 time points using composite sampling, and viral genome concentrations were measured using qRT-PCR.

As shown in Figure 3, genome concentrations of both VSV-GP and VSV-GP^{UV} decreased rapidly (>99.9% cleared the blood) within 1 h and then plateaued between 1 and 3 h. After the 3 h time point, VSV-GP and VSV-GP^{UV} concentrations diverged with concentrations of live virus increasing over the next several hours, peaking at 9 h, and then decreasing through 1 week. By contrast, concentrations of the tool virus continued to rapidly decline after 3 h through 1 week. Trace genome concentrations (∼6 logs lower than C$_{max}$) for both test articles converged near the limit of quantification (LOQ) by 1 week. The concentration-time profile was then split into two phases at an inflection point we observed at the 1 h time point: an early distribution phase (0–1 h) and a late replication-elimination phase (1–168 h). Analysis of variance (ANOVA) demonstrated that the early distribution phase profiles of VSV-GP and VSV-GP^{UV} were not significantly different (p = 0.1861), whereas the replication-elimination phase profiles were significantly different (p < 0.0001).

We calculated PK parameters for both phases using noncompartmental analysis (NCA) in WinNonlin (Table 1). In the early distribution phase, PK parameters were similar between VSV-GP and VSV-GP^{UV} and the volume of distribution (V$_d$) for both viruses was near the approximate total blood volume of BALB/c mice.[61] By contrast,

most parameters differed in the late phase; notably, live VSV-GP exhibited a slower CL rate, later T$_{max}$, greater C$_{max}$, and larger AUC. Of note, concentration measurements for live virus in the late phase capture both input and replicated drug, thus confounding the interpretation of some late-phase PK parameters (e.g., CL and V$_d$).

Finally, as AUC is a measure of exposure, we compared the exposure to replicating (live) versus non-replicating (UV) virus. As noted in Table 1, we approximated AUC from time zero to the final time point (AUC$_{0-t}$) for each test article. We then calculated exposure as a ratio, AUC$_{0-t(live)}$/AUC$_{0-t(UV)}$ (AUC$_R$), to quantify the fold increase in exposure contributed by genomic replication in blood. The calculated AUC$_R$ was 48 (i.e., a 48-fold higher exposure for live virus), indicating that replication significantly impacted systemic exposure (p < 0.0001). In addition, we calculated the absolute exposure directly contributed by replication by subtracting AUC$_{0-t(live)}$-AUC$_{0-t(UV)}$ (ΔAUC). The ΔAUC in blood was 2 × 10^9 genome copies (gc)/mL*h.

Based on the above, we wanted to investigate whether the genomic replication resulted in generation of infectious virus progeny. For this, we performed TCID$_{50}$ analysis on the same blood samples that were assayed for genome copies (Figure 3). As expected, no TCID$_{50}$ activity was detected in mice dosed with VSV-GP^{UV} at any time point (data not shown). For mice dosed with live VSV-GP, TCID$_{50}$ concentration decreased rapidly within the first hour. During this time, the ∼log$_{10}$-fold ratio between genome copies and TCID$_{50}$ concentration for the live virus was consistent with the genome-to-TCID$_{50}$ ratio of the starting test article (∼20-fold). The maintenance of this ratio
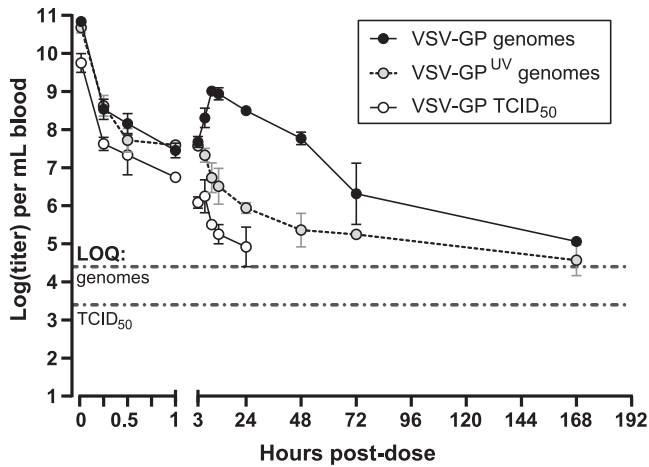
Figure 3. Blood PK of VSV-GP and VSV-GP^{UV}

Concentrations of VSV-GP or VSV-GP^{UV} in mouse whole blood following i.v. injection of 2×10^{10} genome copies (equivalent to 10^9 TCID$_{50}$ for live VSV-GP). Viral titers were determined by qRT-PCR (to measure genome copies) and TCID$_{50}$ assay (to measure infectious units). Data points represent the geometric mean (± geometric SD) of three animals (n = 3), which are plotted against time. The x axis (time) is discontinuous for facile visualization of the distribution phase in the first hour post-dose. qRT-PCR for each animal was performed in technical triplicates. TCID$_{50}$ measurements per animal were performed in duplicate. TCID$_{50}$ assays for all samples from mice dosed with VSV-GP^{UV} were negative (below LOD ~10 TCID$_{50}$/mL) and are not plotted in the graph. SD, standard deviation; LOQ, limit of quantification; LOD, limit of detection.

suggests that CL during this time is due, predominantly, to virus leaving the blood compartment and entering tissues rather than continuously infecting circulating blood cells or being inactivated by serum factors. After the first hour, TCID$_{50}$ concentration continued to decrease and fell below the LOD after 24 h, except for trace amounts (<LOQ) in two mice (~10^2 per mL): one at 48 h and another at 72 h (not graphed). This result suggests that the increase in genomes detected in blood for the live virus was *abortive* genomic replication and resulted in little to no production of extracellular infectious progeny (which would have been indicated by increasing TCID$_{50}$ values or a milder elimination slope compared with genome copy values of the tool virus).

Next, we calculated PK parameters for VSV-GP using TCID$_{50}$ concentration in the early and late phases and then compared them with the PK parameters obtained using genome copies. As shown in Table 1, PK parameters (T$_{max}$, t$_{1/2}$, V$_d$, and CL) derived using TCID$_{50}$ concentrations were similar to PK parameters using genome copies for both VSV-GP and VSV-GP^{UV} in the early phase. In the late phase, TCID$_{50}$ PK parameters were distinct compared with genome copy parameters for live VSV-GP (and VSV-GP^{UV}). Interestingly, CL rates for TCID$_{50}$ were even greater than CL rates for VSV-GP^{UV} genomes in the late phase. This could be explained by the existence of an additional clearance mechanism(s) for TCID$_{50}$ values (e.g., infectious virions entering circulating blood cells). This is consistent with the notion that TCID$_{50}$ values are lost upon entering

cells, whereas genome copy values are retained (i.e., "free" infectious particles are no longer detectable upon binding/entering cells, but its genomes remain detectable).

Tissue BD and PK of VSV-GP and VSV-GP^{UV}

Given that most virus clears rapidly from blood within the first hour, we next investigated the fate of this material after leaving the blood compartment. Tissue samples from spleen, liver, lung, and kidney were collected at six different time points, and viral genomes were measured at each time point using qRT-PCR. To evaluate systemic BD, we selected the earliest time point sampled (1 h) and performed a mass balance to assess the percent of input dose (%ID) distributed across all tissues and blood. As shown in Figure 4A, the predominant sites of distribution for both VSV-GP and VSV-GP^{UV} virus were liver and, to a lesser extent, spleen. These two organs accounted for ~65%–90% of the ID. By contrast, lower levels of distribution were observed in the lung, kidney, and blood (<0.1% ID). We note that, as animals were not perfused prior to sample collection, trace genome concentrations in blood may contribute (albeit minimally) to tissue concentrations.

Next, we assessed tissue PK by analyzing the genome concentrations of VSV-GP and VSV-GP^{UV} in each tissue over time. As shown in the concentration-time profiles in Figures 4B–4E, genome concentrations were similar between VSV-GP and VSV-GP^{UV} at the 1 h time point in all tissues, confirming that early tissue distribution of virus was not impacted by UV irradiation. Thereafter, the concentrations of live and UV-inactivated virus diverged as the live virus genome concentrations increased in all tissues (to varying degrees), except for the liver where genomes decreased slightly.

PK parameters were assessed for tissues using the genome copy values (Table 2). As shown, PK parameters differed between VSV-GP and VSV-GP^{UV} in all analyzed tissues. Notably, live VSV-GP exhibited a higher C$_{max}$, later T$_{max}$, longer t$_{1/2}$, and larger AUC in nearly all tissues (the exception being VSV-GP T$_{max}$ values in liver, which were similar). Interestingly, t$_{1/2}$ values were comparable among tissues for each virus. We surmise that t$_{1/2}$ values at these time points may reflect RNA metabolism rates, which may be conserved across tissues (e.g., by nonspecific cytoplasmic/endosomal RNases).[63]

As in blood, we wanted to quantify the fold change and absolute exposure directly contributed by replication in each tissue by calculating AUC$_R$ and ΔAUC. As shown in Table 2, AUC$_R$ varied across tissues, with spleen exhibiting the highest value (97.1), followed by kidney (33.4), lung (24.5), then liver (4.2). Similar to AUC$_R$, ΔAUC varied across tissues and directly correlated to both the relative BD and extent of genomic replication in each tissue (spleen > liver > lung > kidney). Based on these findings, we conclude that viral replication impacts exposure in healthy mouse tissues to varying extents, as the tissues exhibit variability in their permissivity to virus replication.

Finally, we investigated whether the replication observed in tissues resulted in detectable generation of infectious virus progeny. For this, we measured TCID$_{50}$ over time in tissue homogenates. As shown in

Table 1. Approximated whole-blood PK parameters in the early and late disposition phases

	Analyte	Parameter[a]					
		C_{max} (units/mL)[b]	CL (mL/h)	V_d (mL)	$t_{1/2}$	AUC_{0-t} (units/mL*h)[b]	T_{max}
Early phase	VSV-GP genomes	6.9×10^9	21.8	1.21	12.3 min	4.6×108	1 min
	VSV-GP^{UV} genomes	5.0×10^9	28.3	1.68	6.4 min	3.5×108	1 min
	VSV-GP TCID$_{50}$	6.3×10^8	22.9	1.59	14.6 min	4.4×107	1 min
Late phase	VSV-GP genomes	1.0×10^8	6.0	119.3	11.9 h	1.7×109	9 h
	VSV-GP^{UV} genomes	1.0×10^8	282.8	3,272.5	45.9 h	3.5×107	1 h
	VSV-GP TCID$_{50}$	2.5×10^5	594.1	5,570.3	11.2 h	1.7×106	3 h

[a]C_{max}, maximum concentration; CL, systemic clearance; V_d, volume of distribution; T_{max}, time of maximum concentration; $t_{1/2}$, half-life, AUC_{0-t}, area under the concentration-time curve from starting time (0 for early phase and 1 h for late phase) to time t (1 h for early phase and 168 h for late phase). Parameters were approximated using noncompartmental analysis of concentration-time profiles with mean concentrations from sparse sampling datasets. Concentration at time zero (C_0) was extrapolated for early phase approximations.
[b]Concentration units for total virus genomes and infectious virus genomes are gc/mL or TCID$_{50}$/mL, respectively.

Figures 4B–4E, infectious virus was detected at low levels in all tissues at the 1 h time point. TCID$_{50}$ values in liver, lung, and kidney rapidly decreased near or below the LOQ by 24 h. Conversely, TCID$_{50}$ values in the spleen transiently increased 5.6-fold (p = 0.041) between 1 and 6 h before decreasing below the LOQ by 72 h. This result corroborates previous findings with wild-type VSV by Breitbach et al. (as measured by plaque assay).[29] The low concentrations and rapid clearance of TCID$_{50}$ suggest that genomic replication in healthy tissues did not result in persistent generation of virus progeny (as would be expected in the case of tumor tissue), with the potential exception of spleen, which may support transient and low-level productive replication.

In situ localization and replication dynamics of VSV-GP and VSV-GP^{UV} in tissues

Considering the differences observed in PK parameters between tissues, we sought to further investigate viral replication dynamics *in situ*. For this, we developed strand-specific ISH methods against VSV-GP RNAs, which enabled localization of both antisense (negative-strand) genomes and sense (positive-strand) intermediary viral RNAs independently (Figure 5A). Applying this technique to both VSV-GP and VSV-GP^{UV} allowed us to differentiate the sub-tissue location of input virus genomes and the spatiotemporal dynamics of negative- and positive-strand viral RNA amplification.

We focused on liver and spleen, given that these tissues sequestered the highest levels of dosed virus and yet showed distinct PK profiles. In the liver, input negative-strand genomes were detected at 1 h with similar magnitude and localization for VSV-GP and VSV-GP^{UV} (Figure 5B). This result indicates that distribution and trafficking of the input (negative-strand) virus is independent of replication in the liver, as input distribution of VSV-GP was recapitulated with VSV-GP^{UV}. For both viruses, RNA localized specifically to the cytoplasm of stellate-shaped mononuclear cells within the sinusoidal/perisinusoidal spaces (Kupffer cells). The identification of these cells was confirmed using IHC for a prototypic Kupffer cell marker, F4/80, as well as the prototypic sialic acid receptor, CD169, which is variably expressed (or

induced) by a subset of Kupffer cells (Figure S5).[64] No ISH signal was observed in mature hepatocytes or endothelial cells.

Positive-strand RNA, in contrast, was observed only in mice treated with live VSV-GP. Within this group, positive-strand signal was present starting at the 1 h time point, confirming that transcription/antigenomic replication occurs rapidly in the liver following i.v. dosing. Levels of both positive-strand RNA (VSV-GP) and negative-strand RNA (VSV-GP and VSV-GP^{UV}) decreased by 6 h post-dosing, with only rare ISH staining in the liver by 24 h. At all time points, negative- and positive-strand RNAs localized mainly to CD169$^+$ cells (Figure S5). These results demonstrate that liver macrophages rapidly capture virus from the blood and support a transient burst of positive-strand amplification. Notably, this burst did not result in negative-strand genomic replication (or persistent generation of virus progeny, based on the corresponding TCID$_{50}$ values in the liver).

Next, we examined viral RNA localization over time in the spleen (Figure 5C). At 1 h, we observed input negative-strand genomic RNA for both VSV-GP and VSV-GP^{UV} predominantly in the splenic marginal zone (MZ), which surrounds the lymphocyte-rich areas of white pulp and contains CD169$^+$ macrophages.[65] The distribution and magnitude of VSV-GP and VSV-GP^{UV} negative-strand RNA signals were similar at 1 h, indicating that, as in the liver, the initial BD of VSV-GP^{UV} recapitulated the input live virus in spleen (and that genomic replication of VSV-GP had not occurred by 1 h). At 1 h, positive-strand RNA was observed predominantly in MZ regions, and only in mice dosed with live VSV-GP (Figure 5D). In this group, the positive-strand signal was more abundant compared with the negative-strand signal at 1 h, indicating rapid transcription/antigenomic replication (Figures 5C and 5D, top panels). By 6 h, both negative- and positive-strand RNA signals increased in the MZs of mice dosed with VSV-GP, whereas the negative-strand genome signal decreased in VSV-GP^{UV}-treated mice. By 24 h post-dosing with VSV-GP, the signal for both positive- and negative-strand RNAs had decreased overall and shifted further from the MZs into deeper regions of white pulp (i.e., closer to the central arterioles). The loss of VSV-GP RNA signal in the MZs coincided with lower cellularity
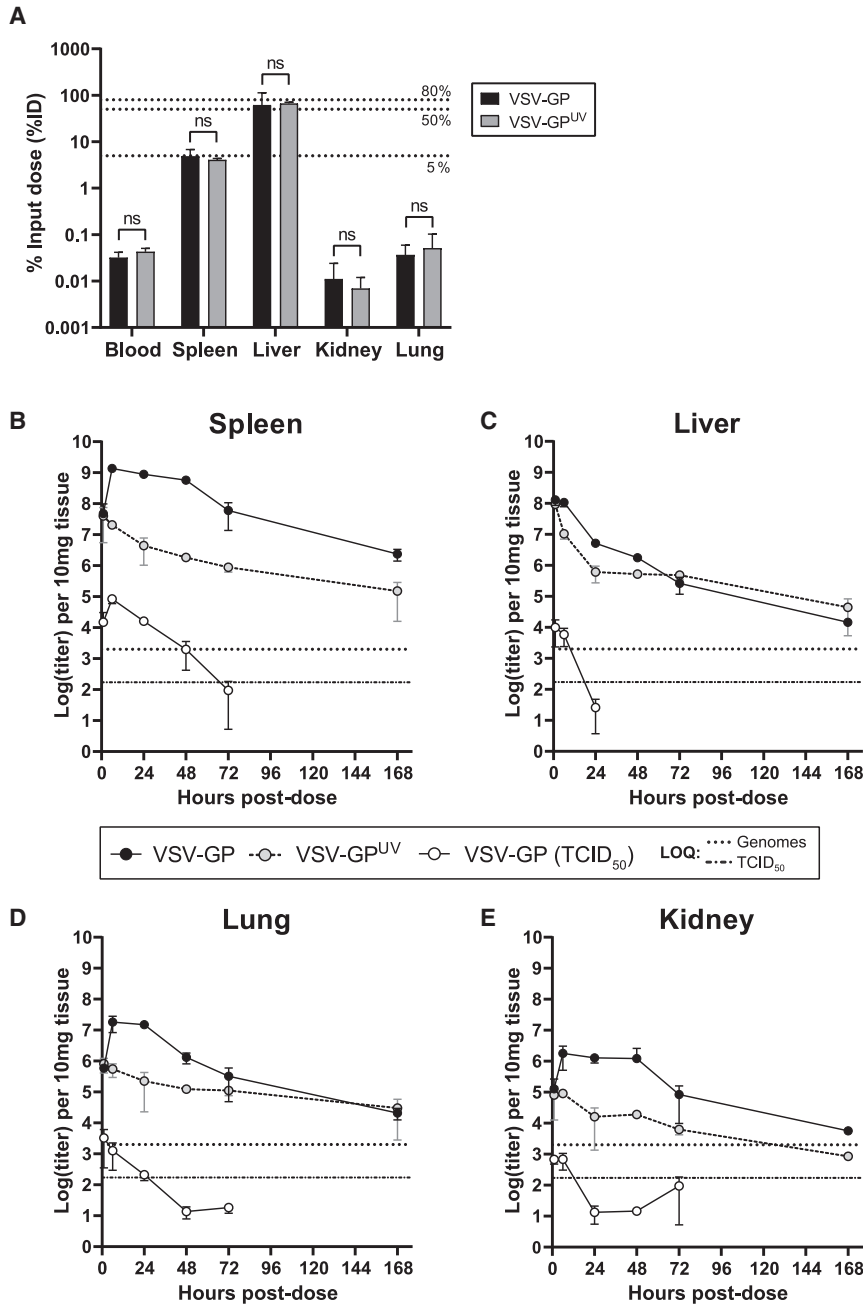
Figure 4. Biodistribution and tissue PK of VSV-GP and VSV-GP^{UV} in mouse tissues

(A) Systemic input dose biodistribution at 1 h post-infection in blood and select tissues (spleen, liver, lung, and kidney). Percent input dose (%ID) was approximated using average female BALB/c organ weights and the average total blood volume[62] to approximate total genomes in each tissue and then dividing by the input genomic dose. Bars represent mean %ID (error bars ±95% CI). (B–E) Mass-normalized biodistribution kinetics in spleen (B), liver (C), lung (D), and kidney (E). Mice received 2×10^{10} genomes of either test article via bolus i.v. injection (10^9 TCID$_{50}$ equivalent to the live test article). Concentration-time profiles were generated by measuring viral genomes by qRT-PCR and infectious units by TCID$_{50}$ assay of tissue homogenates collected at necropsy 1, 6, 24, 48, 72, or 168 h post-dose. Data points represent mean concentrations (±SD) from n = 3 animals per time point. LOQ, limit of quantification; ns, not significant at $\alpha = 0.05$ (unpaired Student's t test); CI, confidence interval.

ous reports that residual VSV genomic RNA can persist in lymphoid organs in the absence of active replication.[33]

Cell-specific IHC markers were used to further define the cell type(s) responsible for VSV-GP uptake and replication in the splenic MZ. As noted, the splenic MZ is populated by macrophages expressing CD169, which we probed by IHC in combination with viral RNA ISH. As shown in Figure 5E, positive-strand VSV-GP RNA at 6 h colocalizes with CD169, confirming that *in vivo* replication of VSV-GP occurs predominantly within this subset of macrophages in the spleen. This observation is concordant with previous findings by Honke et al., who demonstrated that CD169$^+$ MZ macrophages permit "enforced" replication of wild-type VSV as a mechanism to activate adaptive immune responses.[66] As MZ macrophages share similar functions with subcapsular lymph node macrophages during infections,[67] we assessed inguinal and mandibular lymph nodes for viral RNAs in duplex with CD169 (Figure S7). Similar to spleen, both negative- and positive-strand RNAs were detected in CD169$^+$ cells by 1 h and increased in magnitude by 6 h. This finding was indicative of distribution to, and transcription/replication in, lymph node subcapsular macrophages. Genomic replication was confirmed and quantified by qRT-PCR and this replication was determined to be abortive by TCID$_{50}$ analysis (Figure S7). In the other remaining tissues (lung and kidney), viral RNAs were also observed primarily colocalizing with tissue-resident macrophages, although

and scattered cell debris throughout the MZs, suggesting lysis of resident macrophages following VSV-GP uptake. In comparison, in the VSV-GP^{UV} group, negative-strand genomes were largely absent by 24 h. These results demonstrate that a transient burst of VSV-GP replication occurs in the splenic MZs during the initial 24 h post-dosing. By 72 h and through 168 h (168 h seen in Figure S6), scattered residual VSV-GP negative-strand signal was observed mainly within the interior regions of the white pulp; however, scant to no positive-strand RNA was detected. This latter finding is consistent with previ-

Table 2. Tissue biodistribution kinetic parameters

	Analyte	Parameter[a]					
		C_{max} (units/10 mg)[b]	T_{max} (h)	$t_{1/2}$ (h)	AUC_{0-t} (units/10 mg*h)[b]	ΔAUC[c] (gc/10 mg*h)	AUC_R[d]
Spleen	VSV-GP genomes	1.4×10^9	6	16.4	5.2×10^{10}	5.1×10^{10}	97.1
	VSV-GP^{UV} genomes	4.0×10^7	1	31.0	5.4×10^8		
	VSV-GP TCID$_{50}$	8.4×10^4	6	6.4	1.4×10^6		
Liver	VSV-GP genomes	1.3×10^8	1	17.3	1.7×10^9	1.3×10^9	4.2
	VSV-GP^{UV} genomes	6.3×10^7	1	35.9	4.1×10^8		
	VSV-GP TCID$_{50}$	9.9×10^3	1	2.4	8.6×10^4		
Lung	VSV-GP genomes	1.8×10^7	6	16.7	5.8×10^8	5.5×10^8	24.5
	VSV-GP^{UV} genomes	5.5×10^5	1	52.4	2.4×10^7		
	VSV-GP TCID$_{50}$	3.3×10^3	6	11.8	2.8×10^4		
Kidney	VSV-GP genomes	1.8×10^6	6	17.6	8.2×10^7	7.9×10^7	33.4
	VSV-GP^{UV} genomes	9.1×10^4	1	31.4	2.5×10^6		
	VSV-GP TCID$_{50}$	6.8×10^2	1	47.3	2.0×10^4		

[a]C_{max}, maximum concentration; T_{max}, time of maximum concentration; $t_{1/2}$, terminal half-life; AUC_{0-t}, area under the concentration-time curve from time 0 to time t (time t is 168 h for tissues). Parameters were approximated using noncompartmental analysis of concentration-time profiles with mean concentrations from sparse sampling datasets.
[b]Concentration units for total virus genomes and infectious virus genomes are gc/10 mg or TCID$_{50}$/10 mg, respectively.
[c]ΔAUC was calculated by subtracting $AUC_{0-t(live)}$-$AUC_{0-t(UV)}$ calculated based on genome copies only.
[d]AUC_R was calculated by taking the quotient $AUC_{0-t(live)}/AUC_{0-t(UV)}$, calculated based on genome copy values.

ISH-positive cells were sparse in these tissues in comparison with the liver and spleen (Figure S7).

Having observed marked qualitative differences between liver and spleen, we next examined replication/transcription dynamics and tissue innate immune responses *in situ*. First, we quantified VSV-GP and VSV-GP^{UV} ISH signals over time using image analysis. As shown in Figure 5F, negative- and positive-strand RNA kinetics for the live virus in liver were significantly different (p < 0.001) due to greater positive-strand RNA signals at 1 and 6 h. In spleen, per-unit area signal levels for both strands of the live virus were generally greater than in liver. Interestingly, both strands amplified with similar kinetics in the spleen; however, positive-strand RNA was dominant (but not found to be significantly different, p = 0.09) in the early time points (1 and 6 h) and then cleared earlier. This finding is consistent with the expected proportions of VSV RNA strands early in the infection life cycle (i.e., greater amounts of positive-sense VSV-N mRNA transcripts and antigenomes precede negative-sense genome replication).[68] By 24 h and through 168 h, there were no significant differences observed between strands in either liver (p = 0.9) or spleen (p = 0.1).

To investigate whether the tissue-specific difference in permissivity was associated with innate immune responses, we probed the liver and spleen for IFN-β mRNA using ISH to compare innate activation in response to VSV-GP and VSV-GP^{UV} (Figure S8). IFN-β signal localized primarily to cells in which negative- and positive-strand RNAs were found: CD169$^+$/F480$^+$ macrophages in liver (Figure S5), CD169$^+$/F480$^-$ macrophages in spleen (Figures 5E and S6). We then quantified the IFN-β response signals in liver and spleen (Figure 5G). In the liver, the highest level of IFN-β signal was detected

at 1 h. Early responses to VSV-GP trended higher than VSV-GP^{UV}, but the differences in responses were found to not be significantly different (p = 0.4). In the spleen, the IFN-β response was detected at low levels by 1 h and increased by an order of magnitude at the 6 h time point, before returning to baseline at 24 h. In contrast with liver, the spleen IFN response to live VSV-GP was significantly higher than VSV-GP^{UV} (p = 0.0003) despite a delayed onset. These results demonstrate that IFN-β response correlates with replication and permissivity (and thus PK/BD) *in vivo*.

DISCUSSION

Applying classical PK principles to replication-competent OVs necessitates unique considerations as the drug's effect (PD) increases its own concentration (PK/BD), thus making exposure-response relationships challenging to define. Studies to date exploring PK and BD of OVs do not differentiate between the input virus and replicated virus (which can mask input virus exposure), thus confounding standard PK and BD analysis. Toward addressing these considerations, we decoupled the PK and BD of VSV-GP to independently examine its primary (PK^1) and secondary (PK^2) PK profiles. This approach enabled use of quantitative techniques to describe OV fate *in vivo*. The utility of this approach was demonstrated by both enabling application of standard PK principles to a replication-competent vector and elucidating newly proposed PK parameters to account for viral replication (ΔAUC and AUC$_R$).

This approach required thorough development of a replication-incompetent tool virus that retained other critical attributes of the drug to elucidate the PK^1 profile. We focused on optimizing UV irradiation, as it had been reported to minimally impact viral antigenicity and entry for some viruses (presumed determinants of BD).[69,70]
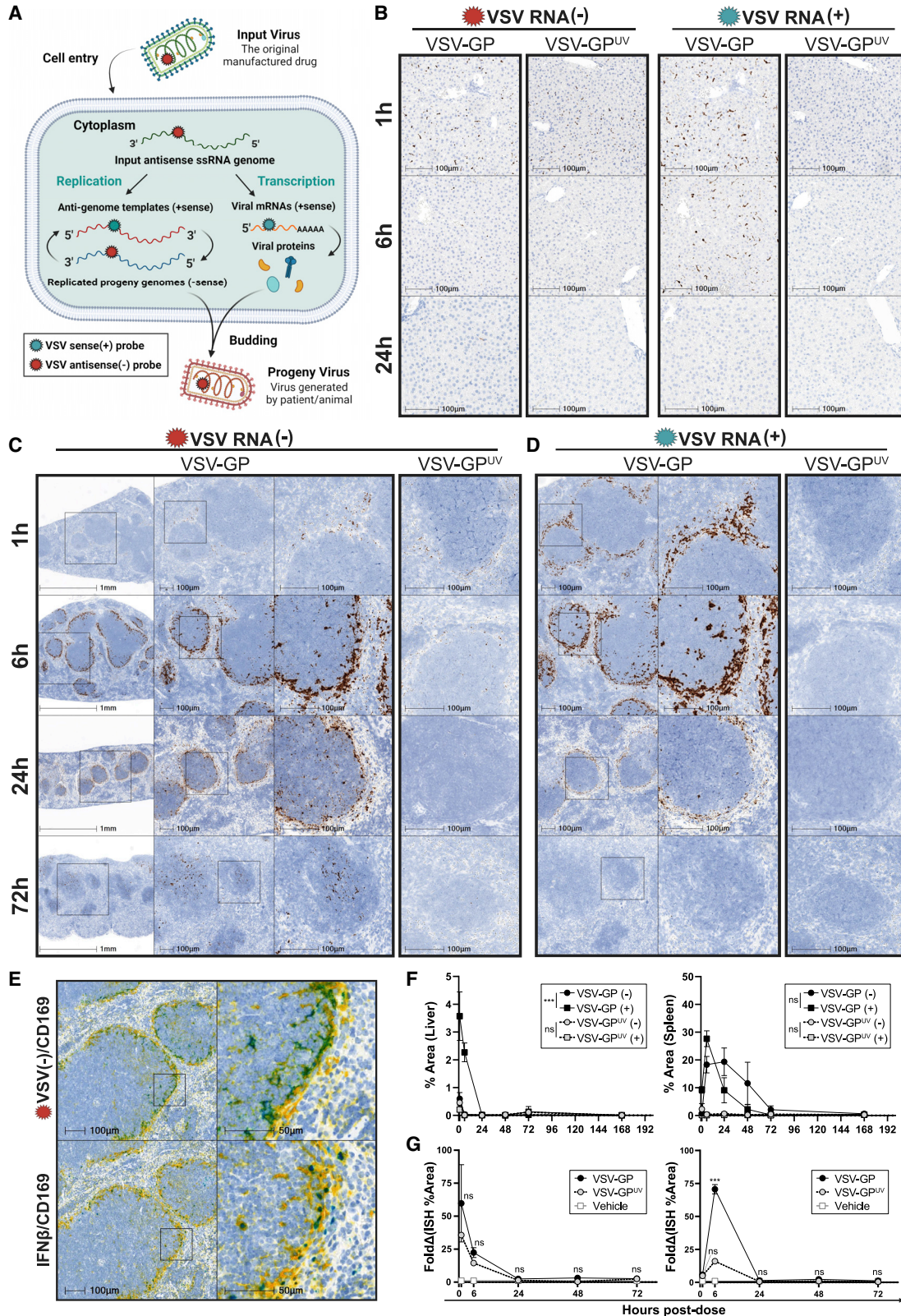
Treatment with UV abrogates infectivity of RNA viruses primarily by damaging their genome—specifically by inducing crosslinks between adjacent uracil (U) residues and between RNA and proteins in an exposure- and wavelength-dependent manner.[53,71] Our early experiments revealed that qRT-PCR genomic recovery was sensitive to UV, confirming previous findings.[71] Thus, the inactivation process required careful optimization to balance genome recovery and infectivity ablation. The final conditions resulted in an inactivated tool virus with minimal perturbations to other critical qualities and equivalent detectability in our specific assays.

When dosed in mice, the tool virus mimicked the input disposition of the live virus in the early phase, which was characterized by rapid blood clearance and tissue uptake. Thereafter, the concentration-time profiles in blood and tissues diverged due to transient viral transcription/replication which impacted all PK and BD parameters in the late phase. This finding demonstrates the ability for healthy non-tumor tissues to permit transient viral transcription/replication, an important consideration when designing and interpreting preclinical safety and pharmacology studies. Variability in tissue permissivity to replication was quantified using AUC_R calculations, whereas ΔAUC calculations provided absolute measurement of exposure differences that account for variable distribution and persistence levels across tissues. As ΔAUC and AUC_R quantify viral replication—and thus measure the drug's effect—these parameters could serve as quantitative PD biomarkers for replication (e.g., enabling comparison between OV candidates and disease models to inform pharmacology and safety). Future studies will apply these approaches to assess and compare replication in tumor-bearing mice. We anticipate that tumor permissivity and efficacy would correlate directly with ΔAUC and AUC_R in the tumor, and that their values may be orders of magnitude higher in permissive tumors compared with healthy tissues.

Although replication was detected in healthy tissues and blood, it was largely found to be abortive in nature, as demonstrated by the lack of secondary progeny detected by $TCID_{50}$ assay (with the notable exception of the spleen). In addition, we found that both input virus and viral transcription/replication was localized in and restricted to tissue-resident macrophages in the assessed tissues. Together, the mass balance approximations (accounting for ~85%–90% of the input dose at 1 h) combined with the fact that input virus colocalized

almost exclusively with tissue macrophages, suggest that specific LCMV-GP interactions with its target receptor may not be the major driver of systemic VSV-GP BD. This observation would be in line with previous observations demonstrating lack of LCMV muscle tropism, despite muscle tissue expressing high levels of αDG.[72–74] In the case of spleen, MZ macrophages specifically served as a site for transient viral replication. In addition, we note that the marked differences in replication (and thus AUC_R) observed between spleen and liver inversely correlated with their relative IFN-β levels at early time points. In the liver, IFN-β response peaked early in response to input virus, whereas a delayed response was observed in spleen, suggesting that the liver macrophages respond more rapidly to input virus and that IFN-β dynamics play a role in tissue permissivity. Collectively, these findings indicate that, for systemically administered VSV-GP, tissue macrophages serve as sentinel immune cells that drive PK^1 and PK^2 in normal tissues. In the blood, we suspect the abortive genomic replication observed also may be driven by circulating monocytes, as peripheral blood mononuclear cells have been previously demonstrated to capture and permit VSV-GP transcription/replication in mice.[75]

In revealing the PK^1 profile of VSV-GP, we demonstrate that its elimination in the absence of replication resembles many inert nanoparticle therapeutics (e.g., short half-life, rapid clearance from blood by liver and the MPS).[76–78] Thus, we infer that the PK^1 properties of an OV are largely driven by its biophysical properties in the early phase, and by RNA metabolism and cellular turnover in the later phase (as the PK^1 elimination profiles in tissues were relatively similar). Moreover, we infer that PK^2 properties are driven by dynamic virus-host interactions (e.g., IFN) that influence replication and thus may be more prone to variability between subjects (relative to PK^1). We also note here that, based on the above, the OV PK field may benefit from tools used to model and modulate nanoparticle PK/PD (especially for PK^1 properties), in addition to using unique tools for addressing viral self-amplification (for interpreting PK^2).

Despite liver and spleen sequestering similar virus concentrations, and exhibiting similar PK^1 profiles, their PK^2 profiles greatly differed (as demonstrated by a nearly 23-fold difference in their AUC_R). Using ISH, we were able to dissect these differences at the cellular level. Macrophages in both tissues captured input virus; however, their responses

Figure 5. In situ analysis of cellular localization and viral replication dynamics of VSV-GP and VSV-GP^UV in liver and spleen
(A) Schematic depicting the targets of the strand-specific ISH probes during the viral life cycle. VSV-GP has a single-stranded antisense (negative strand) RNA genome. Upon cell entry, the genome is transcribed to positive-strand mRNAs and replicated via an intermediary full-length positive-strand antigenomic template. Probes specifically hybridize to either negative- or positive-strand RNAs to differentiate initial input genomes and transcription/antigenomic replication from bona fide genome replication in situ. (B) Strand-specific ISH time course in liver tissue comparing negative-strand (left two panels) and positive-strand (right two panels) for VSV-GP and VSV-GP^UV. (C) Negative-strand (genomic RNA) ISH time course in spleen after dosing with VSV-GP or VSV-GP^UV. Lower magnifications (leftmost column) were used to assess organ-level distribution of viral RNAs and higher magnifications were used to examine RNAs at a cellular resolution. (D) Positive-strand (mRNA and antigenomic RNA) ISH time course in spleen after dosing with VSV-GP or VSV-GP^UV. (E) Duplex ISH (teal)/IHC (yellow) for either negative-strand VSV-GP RNA (top two images) or IFN-β RNA (bottom two images) with CD169 protein in spleen at 6 h post-dose. Colocalization of viral RNA and IFN-β RNA is demonstrated by green areas (or teal surrounded by green and yellow in areas of high ISH expression). (F) Quantification of negative- and positive-strand RNAs on serial sections in mouse spleens over time. Entire slice images from n = 3 mice per time point were assessed for percent hybridized area by image analysis. (G) Quantification of IFN-β RNA in mouse liver (left) and spleen (right) over time. Tissue slice images from n = 3 mice per time point were analyzed to determine percent hybridized area (see Figure S8 for example IFN-β RNA images). All ISH and IHC images shown are representative of three mice per dosing group and time cohort. VSV-N, VSV nucleoprotein; ns, not significant; *p < 0.05; **p < 0.01; ***p < 0.001.

thereafter were markedly different. The role of resident liver macrophages (Kupffer cells) in virus detection and antiviral response has been described previously.[79,80] In our study, we demonstrate their efficiency in shutting down replication after a brief burst of positive-strand amplification (which we presume to be largely mRNA transcription). This brief amplification may result in some of the secondary signal seen in the PK profile. Our findings in spleen and lymph node tissues add credence to the "enforced viral replication" hypothesis described by others—we demonstrate that VSV-GP replicates in CD169^{+} MZ and subcapsular macrophages, corroborating findings with VSV and LCMV and further quantifying their impact on OV PK/BD.[66] Furthermore, CD169^{+} macrophages are known to produce high levels of IFN and interact with dendritic cells to drive adaptive responses, essential mechanisms to control outcomes of viral infections.[81–84] As macrophages are the primary cells driving BD, immunomodulation of these sentinels and their sensing pathways may provide means by which to drive desirable PK and BD properties (i.e., off-targeting liver and spleen toward achieving higher tumor delivery).[85,86]

In summary, the methods used in this study (virus inactivation and ISH-based strand differentiation) were successfully applied toward classical PK and BD analysis of a replication-competent OV. Importantly, the UV-based inactivation approach requires neither additional genetic engineering of the virus (e.g., in the case of single-cycle "ΔG" viruses) nor subsequent purification steps (e.g., to remove chemical inactivators), which could alter important quality attributes that may impact PK/BD or immunogenicity (e.g., aggregates and purity), thus facilitating the use of these approaches on any given drug substance batch and for other virus-based therapeutics. Future directions of this work will focus on employing these techniques to evaluate PK/BD determinants and elucidate PK-PD relationships of replicating OVs and cancer vaccines in disease models.

MATERIALS AND METHODS

Virus propagation and characterization

Virus seed stocks were kindly provided by Dr. Patrik Erlmann (ViraTherapeutics GmbH). Cloning and rescue of VSV-GP has been described previously.[87,88] VSV-GP and VSV-GP-GFP were propagated in HEK293-F suspension cells (Invitrogen, Waltham, MA) in BalanCD medium (FUJIFILM Irvine Scientific, Santa Ana, CA) supplemented with 2% CTS-GlutaMax-I (Thermo Fisher). Cells were infected with virus seed stocks at a low multiplicity of infection (MOI 0.0005) and incubated in shaker flasks in serum-free conditions for 28–32 h. The suspension was harvested, briefly centrifuged to remove cells and debris, and filtered through a 0.2 μm PES filter apparatus. Viruses were then further purified, concentrated, and reformulated using overnight centrifugation ($\sim$16–18 h) at 4,800 × g on a 20% w/v sucrose cushion and nominal temperature of 4°C. Supernatants were carefully decanted, and pelleted virus was resuspended in a Tris-based formulation buffer and stored as single-use aliquots at −80°C. Final virus stocks were characterized using standard viral analytical assays: qRT-PCR to quantify genome copies, TCID$_{50}$ assay to measure infectious titer, and NTA to measure particle size and concentration (method details in subsequent sections).

Virus inactivation

Viruses were inactivated with UV$_{254}$ irradiation in a standard UV crosslinker (Fisherbrand, Waltham, MA) with G8T5 UV-C bulbs (Ushio, Cypress, CA). VSV-GP stocks in formulation buffer were added at 100 μL per well in sterile low-binding polypropylene 96-well plates. To minimize intensity, three (of five) adjacent bulbs were removed from the crosslinker and viruses were shielded by a semi-transparent polypropylene plastic lid. UV intensity was measured with a UV radiometer (Analytik Jena, Jena, Germany). Viruses were exposed for varying lengths of time. Sixty seconds of UV exposure ($\sim$350–450 mJ/cm^2) was selected for generating tool virus for *in vivo* studies. For heat inactivation, VSV-GP was heated to 70°C for 10 min in a thermal block.

NTA

NTA measurements were performed using a NanoSight NS300 instrument with a 405 nm laser and sCMOS camera (Malvern Panalytical, UK). Virus samples were thawed at room temperature and diluted into the linear range of the instrument (20–100 particles in the viewing field, equivalent to $\sim$10^5–10^7 particles/mL). Dilution factors were determined empirically. Samples were then infused into the flow cell using an automated syringe pump at set speed of 75 units for laminar flow. Five 30 s videos were recorded during infusion. Between each capture, the samples were briefly advanced at a set speed of 1,000 units. Additional settings were as follows: camera level 11, detect threshold 6, and temperature 22°C. Fluidics were flushed twice with formulation buffer between samples. Data were analyzed using the manufacturer's software, NanoSight NTA 3.4, and subsequently graphed in GraphPad Prism 9.0 to generate size versus concentration profiles. Final sample concentrations were back-calculated to account for the initial sample dilution.

Cryoelectron microscopy

All samples were imaged undiluted. Each sample was prepared by applying a 3 μL drop of sample suspension to clean 400-mesh copper grids with holey carbon film support, blotting away with filter paper, and immediately proceeding with vitrification in liquid ethane. Grids were stored under liquid nitrogen until transferred to the electron microscope. Electron microscopy was performed using a Thermo Fisher Scientific Glacios Cryo Transmission Electron Microscope operated at 200 kV and equipped with a Falcon 3 direct electron detector. Images of each grid were acquired at multiple scales to assess the overall distribution of the specimen. After identifying suitable target areas for imaging at lower magnifications, high-magnification images were acquired. Images were acquired at a nominal underfocus of −5.5 to −2.0 μm and electron doses of $\sim$25 e$^-$/Å^2.

In vitro cell binding

To assess impacts of UV exposure on cell binding, HEK293-F cells were cooled briefly on ice and then co-incubated with either VSV-GP or VSV-GP^{UV} in sterile low-binding tubes on a rotator inside an incubator at 37°C. At predetermined times post-infection, tubes were removed and centrifuged briefly at 350 × g for 5 min to pellet cells. Supernatant samples were carefully collected for RNA

extraction. Cell binding kinetics were approximated by measuring the depletion of genomes in the supernatant throughout the 1 h incubation time.

In vitro viral kinetics—Cell infection and sample collection

Impacts of UV exposure on the VSV-GP life cycle were measured *in vitro*. To measure replication kinetics, 5×10^5 HEK293-F cells were plated in 12-well tissue culture plates in BalanCD growth medium and incubated overnight in a humidified incubator set to $37°C$ and 5% CO_2 to facilitate cell settling. The next day, cells were pre-cooled on ice for 30 min and infected with viruses in biological duplicates at a nominal MOI of 1 (MOI for UV-inactivated samples was calculated based on their starting $TCID_{50}$ titer prior to inactivation and not final titer). Cell plates were then placed on an orbital shaker set to 200 rpm in a refrigerator set to $4°C$ for 1 h to facilitate virus-cell attachment. After incubation, cells from all wells and plates were collected in a sterile 96-deepwell plate and centrifuged at $300 \times g$ for 5 min at $4°C$. Supernatants were removed, and cells were washed once with ice-cold phosphate-buffered saline (PBS) and centrifuged again to pellet. PBS was removed and cells were resuspended in 1 mL growth medium per well. Each well containing cells was re-plated into 12-well tissue culture plates and placed in an incubator at $37°C$ (5% CO_2) to synchronize viral entry. At predetermined time points post-infection (0, 1, and 30 min, and 1, 2, and 6 h), cell supernatants were collected into sterile polypropylene tubes and centrifuged at $300 \times g$ for 5 min to remove any contaminating cells. Supernatants were then collected into new sterile tubes, flash frozen on dry ice/ethanol, and stored at $-80°C$. Cells were washed once with ice-cold PBS and then each well was lysed with 150 μL buffer RLT (QIAGEN, Hilden, Germany) supplemented with β-mercaptoethanol (Thermo Fisher). Cell lysates were collected, frozen on dry ice, and then stored at $-80°C$.

In vitro viral kinetics—RNA extraction and qRT-PCR to quantify progeny VSV-GP genomes released and intracellular VSV-GP RNA

Supernatant samples were extracted using the QIAamp 96 Viral RNA Kit on a QIAcubeHT extraction system (QIAGEN). Extracted supernatant RNA was analyzed using a one-step qRT-PCR absolute quantification assay for VSV-GP genomes, which is described below. Genome copies were plotted as a function of time in GraphPad Prism 9.0.

Total RNA was extracted from cell lysates using the RNEasy 96 QIAcubeHT kit (QIAGEN) with on-column DNase digestion using the RNase-Free DNase Set (QIAGEN). Total RNA was quantified and qualified on a Big Lunatic spectrophotometer (Unchained Labs) and normalized in all wells to 100 ng/μL with nuclease-free water. One hundred nanograms of RNA per sample was reverse transcribed with an oligo(dT) DNA primer to generate first-strand cDNA using the Superscript IV First-strand Synthesis kit (Thermo Fisher) according to manufacturer's instructions. Reverse transcription was performed at $55°C$. Resulting cDNA was treated with *E. coli* RNaseH (Thermo Fisher) to degrade residual RNA and then subjected to 40 cycles of real-time PCR on a QuantStudio Flex 7 instrument (Applied

Biosystems, Waltham, MA) in fast mode with two reactions: one to detect VSV-N RNA and the other to detect VSV-GP intergenic (M-GP) genomic RNA (described in qRT-PCR for viral genome quantification). Both assays were performed in duplex with a VIC-labeled GAPDH housekeeping gene assay (TaqMan assay ID no. Mm99999915_g1, Thermo Fisher). Reactions were performed in 10 μL total volume in 384-well MicroAmp PCR plates (Applied Biosystems) using TaqMan Fast Advanced Master Mix (Applied Biosystems) in technical triplicates with the following thermocycler settings: 10 min hold at $95°C$ followed by 40 cycles of denaturation at $95°C$ for 1 s and extension at $60°C$ for 20 s. Relative fold-change in gene expression was calculated using the delta-delta-Ct method (fold change = $2^{-\Delta\Delta Ct}$).[89] In brief, target gene Ct values were first normalized to GAPDH and then deltaCt was calculated as the difference compared with time zero. The average of deltaCt values from uninfected cells was then subtracted from the sample deltaCt. Fold-change in VSV-N and VSV-(M-GP) gene expression was plotted as a function of time in GraphPad Prism 9.0.

Sequences for VSV-N RNA assay primer/probes (Life Technologies, Carlsbad, CA) were: forward primer, 5′-TCAAACCATCCGAGC CATTC-3′; reverse primer, 5′-AGTACCGGAGGATTGACGACTAA T-3′; and probe, 5′-(6-FAM)-ACCGCCACAAGGCAGAGATGTGG T-MGB/NFQ-3′. Primers were added at a concentration of 900 nM and probe was added at 250 nM. M-GP intergenic assay primers and probe are described in detail below.

Target receptor and antibody binding assays

The impacts of UV irradiation on virus antigenicity and target binding were assessed using electro-chemiluminescent (ECL) binding immunoassays. In brief, VSV-GP before and after inactivation was coated on Standard Bind plates overnight at $4°C$, blocked with Blocker A solution (Meso Scale Diagnostics (MSD), Rockville, MD), and then probed with either αDG (R&D Systems cat. no. 6868-DG) or anti-LCMV-GP neutralizing antibody, Wen1.3 (internally sourced). For the antibody binding assay, a nonbinding irrelevant antibody (against an irrelevant drug candidate) was used as a negative control. Target binding was detected using an anti-αDG rabbit polyclonal antibody (Sinobiologicals cat. no. 14421-T24) coupled with ruthenium-labeled secondary anti-rabbit IgG (MSD). Antibody binding was detected directly using a ruthenium-labeled anti-mouse IgG (MSD). Washes ($3\times$) were performed between each step using PBS 0.05% Tween 20 (pH 7.4). Plates were read for electrochemiluminescence after addition of read buffer on a MESO QuickPlex SQ 120 reader (MSD). Data were analyzed in the Discovery Workbench instrument software (MSD) and standard curves were curve-fitted using four-parameter logarithmic regression.

IFN release in primary mouse splenocytes

Spleens were harvested from naive 9- to 10-week-old BALB/c mice post-euthanasia and collected into cold RPMI medium supplemented with 2 mM EDTA (Thermo Fisher). Spleens were cut into pieces and gently mashed through a 70 μm nylon mesh and collected in PBS supplemented with 1% fetal bovine serum (FBS)

and $1\times$ penicillin/streptomycin (Thermo Fisher). Cell suspensions were centrifuged at $300 \times g$ for 10 min at $4°C$. Supernatant was removed and red blood cells were then lysed with ACK buffer (Thermo Fisher) with brief pulse vortexing for 3 min. Cells were centrifuged, washed with supplemented PBS, and passed through a 30 μm nylon mesh filter. Cell viability and counts were assessed using a Guava ViaCount (Millipore Sigma, Burlington, MA). Cells were exchanged into culture medium (RPMI, 10% FBS, $1\times$ pen/strep, 10 mM HEPES, $1\times$ NEAA, $1\times$ sodium pyruvate, 55 μM β-ME) (Thermo Fisher) by centrifugation and resuspended to 10^7 viable cells/mL. Splenocytes were plated in 96-well tissue culture plates at 10^6 viable cells/well and incubated overnight in a humidified incubator set to $37°C$ and 5% CO_2. The next day, medium was exchanged and splenocytes were challenged with virus stocks. At pre-determined time points post-infection (12 and 24 h), 100 μL supernatant samples were collected and frozen on dry ice. IFN-α and IFN-β were measured using an MSD U-Plex kit (MesoScale Discovery cat no. K15320K) according to the manufacturer's instructions.

Mouse studies

All animal procedures carried out in this study were performed in accordance with protocols approved by the Boehringer Ingelheim Institutional Animal Care and Use Committee. Female BALB/c mice were procured from Charles River Laboratories (Wilmington, MA). They were 9–10 weeks old at the time of the experiments. Mice were group-housed in individually ventilated cages in a BSL-2 biocontainment facility. Each animal was administered a single bolus intravenous dose of 100 μL VSV-GP, VSV-GP^{UV}, or vehicle via lateral tail vein injection. Both virus-treated groups received 2×10^{10} total viral genomes, equivalent to 10^9 $TCID_{50}$ units for the live virus group and $\leq 10^2$ $TCID_{50}$ units for the VSV-GP^{UV} group. After dosing, the animals were monitored for clinical symptoms at least once daily. Mice were arranged in cohorts by sacrifice time point (n = 3). Each was subjected to one non-terminal bleed and then a terminal bleed and tissue harvest at necropsy. Non-terminal blood sampling was performed by submandibular puncture to collect approximately 100 μL whole blood into K_3EDTA tubes (Sarstedt) at pre-determined time points (1, 15, or 30 min, and 1, 3, 9, or 12 h). Blood was stored on ice for up to 1 h and then frozen at $-80°C$. At predetermined time points (1, 6, 24, 48, 72, or 168 h), mice were humanely euthanized by CO_2 asphyxiation. Terminal blood samples (approximately 250–500 μL) were collected via the vena cava vein in K_3EDTA tubes. Tissues were then collected using aseptic necropsy techniques. Each tissue was thoroughly washed with sterile/RNase-free PBS (Ambion). Prosection tools and wash buffers were changed between mice, and tissues were harvested in order of increasing expected viral RNA levels (determined in pilot studies) to prevent cross-contamination. Each tissue was halved with a fresh razor blade; one-half was placed in 10% neutral buffered formalin (NBF) for IHC and ISH, and the other half was snap frozen in liquid nitrogen for qRT-PCR and $TCID_{50}$.

Viral nucleic acid extraction

Viral nucleic acid was manually extracted from purified virus stocks using the QIAamp Viral RNA Mini kit (QIAGEN) according to the manufacturer's instructions. Viral nucleic acid was extracted from whole-blood samples using either the manual spin-column-based Indispin Pathogen Kit (INDICAL Bioscience, Leipzig, Germany) or the MagMAX Viral/Pathogen Nucleic Acid kit on the KingFisher Flex automation instrument (Thermo Fisher). Finally, viral nucleic acid was extracted from tissues using the QIAamp 96 Virus QIAcube HT kit on the QIAcubeHT automation instrument (QIAGEN). In the case of extracted nucleic acid from biological samples, such as blood and tissues, nucleic acid was quantified and qualified immediately post-extraction using UV-vis spectrophotometry to measure absorbance at 260 nm (A_{260}, nucleic acid concentration), A_{260}/A_{280}, and A_{260}/A_{230} ratios (nucleic acid purity against protein and chemical contaminants, respectively) on a Big Lunatic instrument (Unchained Labs, Pleasanton, CA). Extracted RNA was then analyzed by qRT-PCR immediately or stored at $-80°C$ until analysis.

qRT-PCR for viral genome quantification

Extracted viral RNA samples were subjected to one-step qRT-PCR using a master mix containing Moloney murine leukemia virus reverse transcriptase: TaqMan Fast Virus 1-Step Master Mix (Thermo Fisher). Reaction volumes were either 20 μL (in the case of 96-well plate runs) or 10 μL (in the case of 384-well plate runs) with purified viral RNA comprising one-fourth of the total reaction volume. Single-plex TaqMan qRT-PCR was used to quantify viral genomes using a custom primer/probe set to amplify an intergenic region of the VSV-GP genome (forward primer: 5′-CCTCGAACATGGTCACGATCT-3′; reverse primer: 5′-CCCGGGCTGCAGGAAT-3′; and probe: 5′-(6-FAM)-TCGCCACCATGGGCC-MGB/NFQ-3′). Custom qPCR oligos were designed in Primer Express 3.0.1 (Thermo Fisher) and synthesized by Life Technologies. A synthetic RNA standard was synthesized to generate standard curves for absolute quantitation. First, a DNA plasmid encoding the assay amplicon and flanking regions under T7 promoter control was generated and then used to transcribe a 206-nucleotide synthetic RNA *in vitro* using T7 polymerase (Bio-Synthesis, Lewisville, TX). Lyophilized RNA standard was resuspended in nuclease-free water and quantified by reading A_{260} and utilizing Avogadro's number, molecular weight, and extinction coefficient to convert to copy number. The synthetic RNA standard was stored at $-80°C$ as single-use aliquots at 10^{11} copies/μL in water. Standard curves were generated by serial log-fold dilution of the purified RNA standard in nuclease-free water. The assay is linear over ten orders of magnitude between 50 and 5×10^{10} copies per reaction, and typical runs included either eight (10 to 10^8 copies/μL) or ten (10 to 10^{10} copies/μL) standards in triplicate. Each plate contained at least three no template controls (NTCs), as well as at least one positive extraction control (PEC) and one negative extraction control (NEC), each in triplicate. NTCs contained only nuclease-free water in addition to master mix, primers, and probe. The PEC was prepared by spiking purified virus into a matching biological matrix with each extraction run. NECs were generated with vehicle-treated mice or with naive species-matched tissue specimens (BioIVT, Hicksville, NY). Reverse transcription was performed at $50°C$ followed by 40 cycles of qPCR in fast cycling mode ($95°C$ denaturation for 1 s and $60°C$ extension for 20 s) on a QuantStudio 7 Flex instrument (Applied Biosystems). Data were processed and exported using QuantStudio Real-time PCR

software (Applied Biosystems). A run was considered valid if it met the following criteria: efficiency between 90% and 110%, $R^2 \geq 0.98$, no amplification in NTCs, no amplification in NECs (also acceptable if one triplicate Ct > 39), amplification in all PEC wells, and for PEC of known concentration, accuracy performance must meet: [log10(expected gc/mL)] – [log10(actual gc/mL)] ≤ 1.

TCID$_{50}$ assay

Viral titers were measured in stocks and unknown biological samples (whole-blood and tissue homogenates) with a TCID$_{50}$ assay in BHK-21 cells. Virus stocks and blood were thawed at room temperature and then placed on wet ice for preparing assay dilutions. For tissue homogenates, tissues were cut into pieces using a sterile scalpel and/or 2 mm biopsy punches while partially frozen, weighed, and homogenized in ice-cold sterile PBS with sterile stainless-steel beads on a TissueLyser II homogenizer (QIAGEN). Tissue homogenates were kept cold, diluted, and immediately used to infect cells (described below). To characterize the assay performance with mouse samples, purified virus was spiked into naive blood samples or into tissues in PBS prior to homogenization and assessed for their recovery. During sample analysis, three quality control (QC) spike samples at three representative nominal concentrations (10^8, 10^6, and 10^4 TCID$_{50}$/mL) were included for each biological matrix per run. Each run also included a negative control (NC) comprised of naive mouse matrix and a positive control comprised of a purified virus batch of known infectious titer.

BHK-21 [C-13] cells were procured from American Type Culture Collection (ATCC cat. no. CCL-10) and cultured in Glasgow's minimum essential medium (GMEM) supplemented with 4.3% tryptose phosphate broth and 8.7% heat-inactivated FBS (Thermo Fisher). Five thousand cells in 100 μL were added to each well of 96-well tissue-culture-treated microtiter plates and incubated overnight in a humidified incubator set to 37°C and 5% CO$_2$. The next day (~18–24 h post-plating), cells were infected with samples. In brief, samples were diluted in ice-cold growth medium through eleven 0.5log$_{10}$ (in the case of virus stocks) or log$_{10}$ (in the case of biological samples) serial dilutions. Cells were then infected with 100 μL inoculum per well with 8 technical replicates per dilution level. Thus, each 96-well plate contained a single sample. Cells were incubated with sample dilutions for 72 ± 4 h (37°C, 5% CO$_2$) and then scored for CPE by visual inspection in a light microscope and/or tested for viability using PrestoBlue HS (Thermo Fisher). Titers were calculated using the Spearman-Kärber formula.[90]

In situ hybridization

Tissues were fixed in 10% NBF for 18–24 h and then transferred to 70% ethanol for storage. Fixed samples were trimmed, processed using standard histologic procedures, and embedded in paraffin block. Chilled tissue blocks were sectioned at 4 μm at full face onto positively charged slides. Formalin-fixed paraffin-embedded (FFPE) sections were then dried and stored at room temperature until use for IHC or ISH methods.

Single-plex ISH was performed on a Leica BOND RX autostainer. FFPE sections were placed in an incubator at 60°C for 1 h, then added to the BOND RX instrument where they were deparaffinized. Endogenous peroxidase activity was quenched, and target retrieval was performed according to manufacturer protocols (ACD/Bio-Techne, Newark, CA). A commercially available RNAscope LS V-VSV-N probe (ACD no. 453008, 20ZZ) was used to detect positive-stand genomic and N-mRNA. RNAscope LS V-VSV-sense was a custom-designed probe to detect low levels of the negative-strand N-region of VSV genomic RNA (ACD no. 858988, 40ZZ). See Figure S4 for controls and target validation of the strand-specific ISH method. Mouse IFN-β mRNA was detected using the custom-designed probe RNAscope LS Mm-IFNb-No-XHs (ACD no. 1045159, 13ZZ). Probes were detected using the RNAscope LSx Prefilled Brown detection kit (ACD no. 322700). Following protocol completion, slides were then transferred to an automated cover-slipper (Leica XL Stainer) for mounting and allowed to dry prior to imaging.

Immunohistochemistry

All steps for single-plex staining of CD169$^+$ or F4/80$^+$ macrophages were performed on the Leica BOND RX instrument. FFPE sections described above were deparaffinized and run through heat-induced target retrieval using Tris-EDTA (pH 9.0) (ER2, Leica no. AR9640) for 20 min. Endogenous peroxidase activity was quenched with H$_2$O$_2$* for 15 min and non-specific binding was blocked using Protein Block (Agilent X0909) with 10% normal donkey serum (Sigma no. D9663) for 30 min. Either anti-CD169 rabbit polyclonal antibody (Novus no. NBP2-30903) or anti-F4/80 rabbit monoclonal antibody (Abcam no. ab111101, lot GR3299560-3) were diluted to 1 μg/mL in diluent (Dako-Agilent no. S3022-82-2) and incubated for 30 min, followed by Dako EnVision Detection System with anti-rabbit horseradish peroxidase (HRP) secondary incubation for 30 min (Agilent no. K411), color development with 3,3′-diaminobenzidine (DAB)* for 10 min, and hematoxylin* for 5 min (*components of the BOND polymer Refine detection kit, Leica no. AR9640). Upon run completion, slides were removed from the instrument and dehydrated through a series of increasing alcohol percentages, followed by xylene clearing. Slides were then transferred to an automated cover-slipper (Leica XL Stainer) for mounting and allowed to dry prior to imaging. Specificity of the primary antibodies on mouse tissue was verified by staining in expected cell types and lack of staining when substituting a rabbit polyclonal isotype (Abcam no. ab37415) or rabbit monoclonal isotype (Abcam no. ab172730) (data not shown).

Duplex ISH-IHC was performed on a Roche Discovery Ultra instrument (Roche Diagnostics, Basel, Switzerland). In brief, FFPE tissue sections were incubated at 60°C for 1 h and then loaded on the Discovery Ultra. Tissues were deparaffinized and then antigen retrieval was performed using CC1 buffer for 24 min. The combined ISH-IHC method followed ACD standard incubation and temperature recommendations for RNAscope VS Universal HRP Reagent Kit (ACD no. 32200) and RNAscope 2.5 VS probes V-VSV-sense probe (ACD no. 858989, 40ZZ) or Mm-Ifnb1-No-XHs (ACD no. 1045159, 13ZZ). The ISH probes were detected using the mRNA Teal

chromogen (Roche no. 760-256). Dual sequence was selected, and goat Ig (Roche no. 76–6008) was used as block for 1 h, followed by CD169 antibody (Novus no. NBP2-30903) in diluent (Dako-Agilent no. S3022-82-2) at 1 μg/mL for 1 h. The secondary antibody UMap-Rb-AP (Roche 760-4313) was applied for 20 min, followed by the Discovery Yellow chromogen (Roche no. 760-239) for 48 min. Nuclei were detected using Hematoxylin II (Roche no. 790-2208) for 4 min and Bluing (Roche no. 760-2037) for 4 min. Following completion of the staining protocol, slides were washed and then transferred to an automated cover-slipper (Leica XL Stainer) for mounting and drying prior to imaging.

Stained tissue sections were scanned using a Leica AT2 scanner at 20× objective magnification with a doubler inserted to capture the single-plex DAB IHC and ISH markers. Chromogenic duplex ISH-IHC tissue sections were scanned on an Axioscan KMAT (Zeiss no. 494915-9880) with PApo 20×/0.8 M27 objective. See Figure S6 for validation of the ISH/IHC duplex.

Image analysis for RNA quantification

Digital image analysis algorithms were developed in Visiopharm software (Hørsholm, Denmark). The workflow involved separate modules (APPS) to first detect the tissue region of interest (ROI) from background and then isolate the signal at a high resolution (20× magnification). For single-plex ISH images, nuclei and signals from the ISH probes were initially detected inside the ROI. Both nucleus and probe signal detection used image processing filters to enhance their features, such as local gradient and curvature. The nucleus detection was based on a combination of the red, green, and hematoxylin color-deconvolution bands, whereas the detection of the probe signal was based on the hematoxylin and DAB deconvolution bands. The output variables were dark spot area, nuclei area, and tissue area. The algorithm results for negative and positive total ISH area were normalized for each tissue by dividing by total tissue area analyzed for the specimen and graphed as percent tissue area. For IFN-β, normalized percent area results were used to determine fold-change induction of IFN-β compared with vehicle-treated mice at each time point.

PK and statistical analysis

Concentration-time profiles were generated by plotting geometric mean concentrations (± geometric standard deviation) versus time. NCA via the linear-up-log-down trapezoidal method was used to calculate PK parameters, such as total exposure (AUC), clearance (CL), volume of distribution (V_d), maximum concentration (C_{max}), half-life ($t_{1/2}$), and other standard parameters, in Phoenix 64 WinNonlin version 8.3 (Certara, Princeton, NJ). Additional calculations to compare PK^1 and PK^2 profiles, such as ΔAUC and AUC_R, were performed in Microsoft Excel. PK differences between test articles (VSV-GP versus VSV-GP^{UV}) or between compartments were evaluated for statistical significance via Student's t test of the log-transformed parameters (for two groups) or two-way ANOVA ($\geq$ three groups) at a significance level of α = 0.05. Differences in the concentration-time profiles (or %ISH area versus time profiles)

between groups were compared using two-way ANOVA with a mixed-effects model and Geisser-Greenhouse correction (α = 0.05) after log-transformation of the data. Mixed-effects analysis was performed in lieu of two-way ANOVA in cases of excluded data points (one subject removed due to presumed partial dose, three instances of image artifacts). Post-hoc tests were used to compare means at each time point between groups, or to compare differences within groups (in the case of comparing concentrations or ISH responses at different time points). Multiple comparisons tests were performed with Tukey's correction for ANOVA analyses and with Šidák-Dunn correction for mixed-effect analyses. Statistical analyses were performed in Prism version 9.3.1 (GraphPad Software, La Jolla, CA).

DATA AVAILABILITY

Supporting data for this study are available from the corresponding author, J.A., upon reasonable request. Some information specific to VSV-GP and samples thereof may be limited due to restrictions that could compromise proprietary information (neither samples of the vector itself nor its full genetic sequence can be shared at this time).

SUPPLEMENTAL INFORMATION

Supplemental information can be found online at https://doi.org/10.1016/j.omtm.2022.12.013.

AUTHOR CONTRIBUTIONS

R.D., A.M., A.V., C.W., and J.A. conceived and designed the overall research. B.F., C.G., A.V., C.W., and J.A. supervised the research and provided feedback. R.D. wrote the original manuscript and made figures. R.D., A.M., J.M.S., C.W., A.V., and J.A. edited the manuscript. R.D. designed and coordinated *in vivo* and *in vitro* studies. R.D., S.S.A., K.G., A.B.-C., J.M.S., M.M., R.R., and C.M.C. performed *in vivo* experiments. R.D., K.G., S.S.A., A.B.-C., and J.M.S. performed virus production, *in vitro* virology, and bioanalysis of study samples. R.D. performed PK and statistical analyses. S.A. developed and performed binding immunoassays. C.L. and L.C. developed and performed splenocyte cytokine release assays. D.X. coordinated

electron microscopy experiments. A.M., S.M., and C.W. designed, analyzed, and interpreted molecular pathology methods. A.M., S.M., M.W., and K.B. performed molecular pathology experiments. R.D., A.M., A.V., C.W., and J.A. interpreted the overall results of the studies. B.F., C.G., and A.V. secured necessary support for this work.

DECLARATION OF INTERESTS

REFERENCES

1. Andtbacka, R.H.I., Kaufman, H.L., Collichio, F., Amatruda, T., Senzer, N., Chesney, J., Delman, K.A., Spitler, L.E., Puzanov, I., Agarwala, S.S., et al. (2015). Talimogene laherparepvec improves durable response rate in patients with advanced melanoma. J. Clin. Oncol. 33, 2780–2788. https://doi.org/10.1200/jco.2014.58.3377.

2. Haitz, K., Khosravi, H., Lin, J.Y., Menge, T., and Nambudiri, V.E. (2020). Review of talimogene laherparepvec: a first-in-class oncolytic viral treatment of advanced melanoma. J. Am. Acad. Dermatol. 83, 189–196. https://doi.org/10.1016/j.jaad.2020.01.039.

3. Russell, S.J., Federspiel, M.J., Peng, K.-W., Tong, C., Dingli, D., Morice, W.G., Lowe, V., O'Connor, M.K., Kyle, R.A., Leung, N., et al. (2014). Remission of disseminated cancer after systemic oncolytic virotherapy. Mayo Clin. Proc. 89, 926–933. https://doi.org/10.1016/j.mayocp.2014.04.003.

4. Li, Z., Jiang, Z., Zhang, Y., Huang, X., and Liu, Q. (2020). Efficacy and safety of oncolytic viruses in randomized controlled trials: a systematic review and meta-analysis. Cancers 12, 1416. https://doi.org/10.3390/cancers12061416.

5. Lemos de Matos, A., Franco, L.S., and McFadden, G. (2020). Oncolytic viruses and the immune system: the dynamic duo. Mol. Ther. Methods Clin. Dev. 17, 349–358. https://doi.org/10.1016/j.omtm.2020.01.001.

6. Maroun, J., Muoz-Ala, M., Ammayappan, A., Schulze, A., Peng, K.-W., and Russell, S. (2017). Designing and building oncolytic viruses. Future Virol. 12, 193–213. https://doi.org/10.2217/fvl-2016-0129.

7. Aitken, A.S., Roy, D.G., and Bourgeois-Daigneault, M.-C. (2017). Taking a stab at cancer; oncolytic virus-mediated anti-cancer vaccination strategies. Biomedicines 5, 3. https://doi.org/10.3390/biomedicines5010003.

8. Hastie, E., and Grdzelishvili, V.Z. (2012). Vesicular stomatitis virus as a flexible platform for oncolytic virotherapy against cancer. J. Gen. Virol. 93, 2529–2545. https://doi.org/10.1099/vir.0.046672-0.

9. Felt, S.A., and Grdzelishvili, V.Z. (2017). Recent advances in vesicular stomatitis virus-based oncolytic virotherapy: a 5-year update. J. Gen. Virol. 98, 2895–2911. https://doi.org/10.1099/jgv.0.000980.

10. Lundstrom, K. (2018). Self-replicating RNA viruses for RNA therapeutics. Molecules 23, 3310. https://doi.org/10.3390/molecules23123310.

11. Melzer, M.K., Lopez-Martinez, A., and Altomonte, J. (2017). Oncolytic vesicular stomatitis virus as a viro-immunotherapy: defeating cancer with a "hammer" and "anvil". Biomedicines 5, 8. https://doi.org/10.3390/biomedicines5010008.

12. Clarke, D.K., Cooper, D., Egan, M.A., Hendry, R.M., Parks, C.L., and Udem, S.A. (2006). Recombinant vesicular stomatitis virus as an HIV-1 vaccine vector. Springer Semin. Immunopathol. 28, 239–253. https://doi.org/10.1007/s00281-006-0042-3.

13. Liu, Y.-P., Steele, M.B., Suksanpaisan, L., Federspiel, M.J., Russell, S.J., Peng, K.W., and Bakkum-Gamez, J.N. (2014). Oncolytic measles and vesicular stomatitis virotherapy for endometrial cancer. Gynecol. Oncol. 132, 194–202. https://doi.org/10.1016/j.ygyno.2013.11.010.

14. Durham, N.M., Mulgrew, K., McGlinchey, K., Monks, N.R., Ji, H., Herbst, R., Suzich, J., Hammond, S.A., and Kelly, E.J. (2017). Oncolytic VSV primes differential responses to immuno-oncology therapy. Mol. Ther. 25, 1917–1932. https://doi.org/10.1016/j.ymthe.2017.05.006.

15. Zhang, L., Steele, M.B., Jenks, N., Grell, J., Suksanpaisan, L., Naik, S., Federspiel, M.J., Lacy, M.Q., Russell, S.J., and Peng, K.-W. (2016). Safety studies in tumor and non-tumor-bearing mice in support of clinical trials using oncolytic VSV-IFN-β-NIS. Hum. Gene Ther. Clin. Dev. 27, 111–122. https://doi.org/10.1089/humc.2016.061.

16. Naik, S., Nace, R., Federspiel, M.J., Barber, G.N., Peng, K.-W., and Russell, S.J. (2012). Curative one-shot systemic virotherapy in murine myeloma. Leukemia 26, 1870–1878. https://doi.org/10.1038/leu.2012.70.

17. Jonker, D.J., Hotte, S.J., Abdul Razak, A.R., Renouf, D.J., Lichty, B., Bell, J.C., Powers, J., Breitbach, C.J., Stojdl, D.F., Stephenson, K.B., et al. (2017). Phase I study of oncolytic virus (OV) MG1 maraba/MAGE-A3 (MG1MA3), with and without transgenic MAGE-A3 adenovirus vaccine (AdMA3) in incurable advanced/metastatic MAGE-A3-expressing solid tumours: CCTG IND.214. J. Clin. Oncol. 35, e14637. https://doi.org/10.1200/jco.2017.35.15_suppl.e14637.

18. Naik, S., Galyon, G.D., Jenks, N.J., Steele, M.B., Miller, A.C., Allstadt, S.D., Suksanpaisan, L., Peng, K.W., Federspiel, M.J., Russell, S.J., and LeBlanc, A.K. (2017). Comparative oncology evaluation of intravenous recombinant oncolytic Vesicular Stomatitis Virus therapy in spontaneous canine cancer. Mol. Cancer Ther. 17, 316–326. https://doi.org/10.1158/1535-7163.mct-17-0432.

19. Cook, J., Peng, K.-W., Geyer, S., Dueck, A.C., Ginos, B.F., Giers, M., Packiriswamy, N., Zhang, L., Brunton, B., Patnaik, M.S., et al. (2021). TCL-461: clinical activity of systemic VSV-IFNβ-NIS oncolytic virotherapy in patients with relapsed refractory hematologic malignancies. Clin. Lymphoma, Myeloma & Leukemia 21, S416–S417. https://doi.org/10.1016/s2152-2650(21)01935-2.

20. Bolt, M.W., Whiteley, L.O., Lynch, J.L., Lauritzen, B., Fernández de Henestrosa, A.R., MacLachlan, T., Ulrich, P., Philip, B.K., Mahalingaiah, P.K., Fuller, C.L., and Compton, D.R. (2020). Nonclinical studies that support viral vector-delivered gene therapies: an EFPIA gene therapy working group perspective. Mol. Ther. Methods Clin. Dev. 19, 89–98. https://doi.org/10.1016/j.omtm.2020.08.017.

21. (2013). Guidance for Industry: Preclinical Assessment of Investigational Cellular and Gene Therapy Products (Food and Drug Administration Center for Biologics Evaluation and Research).

22. Ganesan, L.P., Mohanty, S., Kim, J., Clark, K.R., Robinson, J.M., and Anderson, C.L. (2011). Rapid and efficient clearance of blood-borne virus by liver sinusoidal endothelium. PLoS Pathog. 7, e1002281. https://doi.org/10.1371/journal.ppat.1002281.

23. LeBlanc, A.K., Naik, S., Galyon, G.D., Jenks, N., Steele, M., Peng, K.-W., Federspiel, M.J., Donnell, R., and Russell, S.J. (2013). Safety studies on intravenous administration of oncolytic recombinant vesicular stomatitis virus in purpose-bred beagle dogs. Hum. Gene Ther. Clin. Dev. 24, 174–181. https://doi.org/10.1089/humc.2013.165.

24. Brunner, K.T., Hurez, D., McCluskey, R.T., and Benacerraf, B. (1960). Blood clearance of P32-labeled vesicular stomatitis and Newcastle disease viruses by the reticuloendothelial system in mice. J. Immunol. 85, 99–105.

25. Byrnes, A.P., and Griffin, D.E. (2000). Large-plaque mutants of sindbis virus show reduced binding to heparan sulfate, heightened viremia, and slower clearance from the circulation. J. Virol. 74, 644–651. https://doi.org/10.1128/jvi.74.2.644-651.2000.

26. Parra-Guillen, Z.P., Freshwater, T., Cao, Y., Mayawala, K., Zalba, S., Garrido, M.J., de Alwis, D., and Troconiz, I.F. (2021). Mechanistic modeling of a novel oncolytic virus, V937, to describe viral kinetic and dynamic processes following intratumoral and intravenous administration. Front. Pharmacol. 12, 705443. https://doi.org/10.3389/fphar.2021.705443.

27. Croyle, M.A., Callahan, S.M., Auricchio, A., Schumer, G., Linse, K.D., Wilson, J.M., Brunner, L.J., and Kobinger, G.P. (2004). PEGylation of a vesicular stomatitis virus G pseudotyped lentivirus vector prevents inactivation in serum. J. Virol. 78, 912–921. https://doi.org/10.1128/jvi.78.2.912-921.2004.

28. Alemany, R., Suzuki, K., and Curiel, D.T. (2000). Blood clearance rates of adenovirus type 5 in mice. J. Gen. Virol. 81, 2605–2609. https://doi.org/10.1099/0022-1317-81-11-2605.

29. Breitbach, C.J., Paterson, J.M., Lemay, C.G., Falls, T.J., McGuire, A., Parato, K.A., Stojdl, D.F., Daneshmand, M., Speth, K., Kirn, D., et al. (2007). Targeted inflammation during oncolytic virus therapy severely compromises tumor blood flow. Mol. Ther. 15, 1686–1693. https://doi.org/10.1038/sj.mt.6300215.

30. Cai, J., Zhu, W., Lin, Y., Zhang, S., Chen, X., Gong, S., He, S., Hu, J., Yan, G., and Liang, J. (2020). Systematic characterization of the biodistribution of the oncolytic virus M1. Hum. Gene Ther. 31, 1203–1213. https://doi.org/10.1089/hum.2020.114.

31. Howard, F., and Muthana, M. (2020). Designer nanocarriers for navigating the systemic delivery of oncolytic viruses. Nanomedicine (Lond) *15*, 93–110. https://doi.org/10.2217/nnm-2019-0323.

32. Junt, T., Moseman, E.A., Iannacone, M., Massberg, S., Lang, P.A., Boes, M., Fink, K., Henrickson, S.E., Shayakhmetov, D.M., Di Paolo, N.C., et al. (2007). Subcapsular sinus macrophages in lymph nodes clear lymph-borne viruses and present them to antiviral B cells. Nature *450*, 110–114. https://doi.org/10.1038/nature06287.

33. Simon, I.D., van Rooijen, N., and Rose, J.K. (2010). Vesicular stomatitis virus genomic RNA persists in vivo in the absence of viral replication. J. Virol. *84*, 3280–3286. https://doi.org/10.1128/jvi.02052-09.

34. Russell, S.J., Peng, K.-W., and Bell, J.C. (2012). Oncolytic virotherapy. Nat. Biotechnol. *30*, 658–670. https://doi.org/10.1038/nbt.2287.

35. Peng, K.-W., Hadac, E.M., Anderson, B.D., Myers, R., Harvey, M., Greiner, S.M., Soeffker, D., Federspiel, M.J., and Russell, S.J. (2006). Pharmacokinetics of oncolytic measles virotherapy: eventual equilibrium between virus and tumor in an ovarian cancer xenograft model. Cancer Gene Ther. *13*, 732–738. https://doi.org/10.1038/sj.cgt.7700948.

36. Pelin, A., Wang, J., Bell, J., and Le Boeuf, F. (2018). The importance of imaging strategies for pre-clinical and clinical in vivo distribution of oncolytic viruses. Oncolytic Virother. *7*, 25–35. https://doi.org/10.2147/ov.s137159.

37. Schreiber, L.-M., Urbiola, C., Erlmann, P., and Wollmann, G. (2020). Oncolytic viruses in vivo bioimaging for monitoring intratumoral virus activity. Methods Mol. Biol. *2058*, 237–248. https://doi.org/10.1007/978-1-4939-9794-7_15.

38. Béguin, J., Gantzer, M., Farine, I., Foloppe, J., Klonjkowski, B., Maurey, C., Quéméneur, É., and Erbs, P. (2021). Safety, biodistribution and viral shedding of oncolytic vaccinia virus TG6002 administered intravenously in healthy beagle dogs. Sci. Rep. *11*, 2209. https://doi.org/10.1038/s41598-021-81831-2.

39. Jing, Y., Zaias, J., Duncan, R., Russell, S.J., and Merchan, J.R. (2014). In vivo safety, biodistribution and antitumor effects of uPAR retargeted oncolytic measles virus in syngeneic cancer models. Gene Ther. *21*, 289–297. https://doi.org/10.1038/gt.2013.84.

40. Johnson, J.E., Coleman, J.W., Kalyan, N.K., Calderon, P., Wright, K.J., Obregon, J., Ogin-Wilson, E., Natuk, R.J., Clarke, D.K., Udem, S.A., et al. (2009). In vivo biodistribution of a highly attenuated recombinant vesicular stomatitis virus expressing HIV-1 Gag following intramuscular, intranasal, or intravenous inoculation. Vaccine *27*, 2930–2939. https://doi.org/10.1016/j.vaccine.2009.03.006.

41. Peng, K.-W., Frenzke, M., Myers, R., Soeffker, D., Harvey, M., Greiner, S., Galanis, E., Cattaneo, R., Federspiel, M.J., and Russell, S.J. (2003). Biodistribution of oncolytic measles virus after intraperitoneal administration into ifnar-CD46Ge transgenic mice. Hum. Gene Ther. *14*, 1565–1577. https://doi.org/10.1089/104303403322495070.

42. Titze, M.I., Frank, J., Ehrhardt, M., Smola, S., Graf, N., and Lehr, T. (2017). A generic viral dynamic model to systematically characterize the interaction between oncolytic virus kinetics and tumor growth. Eur. J. Pharm. Sci. *97*, 38–46. https://doi.org/10.1016/j.ejps.2016.11.003.

43. Kaufman, H.L., Kohlhapp, F.J., and Zloza, A. (2015). Oncolytic viruses: a new class of immunotherapy drugs. Nat. Rev. Drug Discov. *14*, 642–662. https://doi.org/10.1038/nrd4663.

44. Meibohm, B., and Derendorf, H. (1997). Basic concepts of pharmacokinetic/pharmacodynamic (PK/PD) modelling. Int. J. Clin. Pharmacol. Ther. *35*, 401–413.

45. Imlygic Public Assessment Report (2015). European Medicines Agency Committee for Medicinal Products for Human Use.

46. Das, K., Belnoue, E., Rossi, M., Hofer, T., Danklmaier, S., Nolden, T., Schreiber, L.-M., Angerer, K., Kimpel, J., Hoegler, S., et al. (2021). A modular self-adjuvanting cancer vaccine combined with an oncolytic vaccine induces potent antitumor immunity. Nat. Commun. *12*, 5195. https://doi.org/10.1038/s41467-021-25506-6.

47. (2019). Phase 1b Study to Evaluate ATP128, VSV-GP128 and BI 754091, in Patients with Stage IV Colorectal Cancer (KISIMA-01). https://clinicaltrials.gov/ct2/show/NCT04046445.

48. Porosnicu, M., Quinson, A.-M., Crossley, K., Luecke, S., and Lauer, U.M. (2022). Phase I study of VSV-GP (BI 1831169) as monotherapy or combined with ezabenlimab in advanced and refractory solid tumors. Future Oncol. *18*, 2627–2638. https://doi.org/10.2217/fon-2022-0439.

49. Weck, P.K., Carroll, A.R., Shattuck, D.M., and Wagner, R.R. (1979). Use of UV irradiation to identify the genetic information of vesicular stomatitis virus responsible for shutting off cellular RNA synthesis. J. Virol. *30*, 746–753.

50. Whelan, S.P.J., and Wertz, G.W. (2002). Transcription and replication initiate at separate sites on the vesicular stomatitis virus genome. Proc. Natl. Acad. Sci. USA *99*, 9178–9183. https://doi.org/10.1073/pnas.152155599.

51. Abaskharon, R.M., and Gai, F. (2016). Direct measurement of the tryptophan-mediated photocleavage kinetics of a protein disulfide bond. Phys. Chem. Chem. Phys. *18*, 9602–9607. https://doi.org/10.1039/c6cp00865h.

52. Whitaker-Dowling, P., and Younger, J.S. (1988). Alteration of vesicular stomatitis virus L and NS proteins by uv irradiation: implications for the mechanism of host cell shut-off. Virology *164*, 171–175. https://doi.org/10.1016/0042-6822(88)90633-2.

53. Miller, R.L., and Plagemann, P.G. (1974). Effect of ultraviolet light on mengovirus: formation of uracil dimers, instability and degradation of capsid, and covalent linkage of protein to viral RNA. J. Virol. *13*, 729–739. https://doi.org/10.1128/jvi.13.3.729-739.1974.

54. Cao, W., Henry, M.D., Borrow, P., Yamada, H., Elder, J.H., Ravkov, E.V., Nichol, S.T., Compans, R.W., Campbell, K.P., and Oldstone, M.B. (1998). Identification of α-dystroglycan as a receptor for lymphocytic choriomeningitis virus and lassa fever virus. Science *282*, 2079–2081. https://doi.org/10.1126/science.282.5396.2079.

55. Kunz, S., Sevilla, N., McGavern, D.B., Campbell, K.P., and Oldstone, M.B. (2001). Molecular analysis of the interaction of LCMV with its cellular receptor α-dystroglycan. J. Cell Biol. *155*, 301–310. https://doi.org/10.1083/jcb.200104103.

56. Seiler, P., Bründler, M.A., Zimmermann, C., Weibel, D., Bruns, M., Hengartner, H., and Zinkernagel, R.M. (1998). Induction of protective cytotoxic T cell responses in the presence of high titers of virus-neutralizing antibodies: implications for passive and active immunization. J. Exp. Med. *187*, 649–654. https://doi.org/10.1084/jem.187.4.649.

57. Hangartner, L., Zellweger, R.M., Giobbi, M., Weber, J., Eschli, B., McCoy, K.D., Harris, N., Recher, M., Zinkernagel, R.M., and Hengartner, H. (2006). Nonneutralizing antibodies binding to the surface glycoprotein of lymphocytic choriomeningitis virus reduce early virus spread. J. Exp. Med. *203*, 2033–2042. https://doi.org/10.1084/jem.20051557.

58. Zimmer, B., Summermatter, K., and Zimmer, G. (2013). Stability and inactivation of vesicular stomatitis virus, a prototype rhabdovirus. Vet. Microbiol. *162*, 78–84. https://doi.org/10.1016/j.vetmic.2012.08.023.

59. Hidmark, Å.S., McInerney, G.M., Nordström, E.K.L., Douagi, I., Werner, K.M., Liljeström, P., and Karlsson Hedestam, G.B. (2005). Early alpha/beta interferon production by myeloid dendritic cells in response to UV-inactivated virus requires viral entry and interferon regulatory factor 3 but not MyD88. J. Virol. *79*, 10376–10385. https://doi.org/10.1128/jvi.79.16.10376-10385.2005.

60. Collins, S.E., Noyce, R.S., and Mossman, K.L. (2004). Innate cellular response to virus particle entry requires IRF3 but not virus replication. J. Virol. *78*, 1706–1717. https://doi.org/10.1128/jvi.78.4.1706-1717.2004.

61. Species specific information: mouse animal care and use committee. Johns Hopkins University. https://web.jhu.edu/animalcare/procedures/mouse.html.

62. Denegre, J. (2007). Morphometric (Organ Weight) Survey of 11 Strains of Mice (The Jackson Laboratory Mouse Phenome Database (MPD)). http://phenome.jax.org/.

63. Houseley, J., and Tollervey, D. (2009). The many pathways of RNA degradation. Cell *136*, 763–776. https://doi.org/10.1016/j.cell.2009.01.019.

64. Gordon, S., Plüddemann, A., and Mukhopadhyay, S. (2014). Sinusoidal immunity: macrophages at the lymphohematopoietic interface. Cold Spring Harb. Perspect. Biol. *7*, a016378. https://doi.org/10.1101/cshperspect.a016378.

65. Grabowska, J., Lopez-Venegas, M.A., Affandi, A.J., and den Haan, J.M.M. (2018). CD169+ macrophages capture and dendritic cells instruct: the interplay of the gatekeeper and the general of the immune system. Front. Immunol. *9*, 2472. https://doi.org/10.3389/fimmu.2018.02472.

66. Honke, N., Shaabani, N., Cadeddu, G., Sorg, U.R., Zhang, D.-E., Trilling, M., Klingel, K., Sauter, M., Kandolf, R., Gailus, N., et al. (2011). Enforced viral replication activates adaptive immunity and is essential for the control of a cytopathic virus. Nat. Immunol. *13*, 51–57. https://doi.org/10.1038/ni.2169.

67. Louie, D.A.P., and Liao, S. (2019). Lymph node subcapsular sinus macrophages as the frontline of lymphatic immune defense. Front. Immunol. *10*, 347. https://doi.org/10.3389/fimmu.2019.00347.

68. Ogino, T., and Green, T.J. (2019). RNA synthesis and capping by non-segmented negative strand RNA viral polymerases: lessons from a prototypic virus. Front. Microbiol. *10*, 1490. https://doi.org/10.3389/fmicb.2019.01490.

69. Hankaniemi, M.M., Stone, V.M., Sioofy-Khojine, A.-B., Heinimäki, S., Marjomäki, V., Hyöty, H., Blazevic, V., Laitinen, O.H., Flodström-Tullberg, M., and Hytönen, V.P. (2019). A comparative study of the effect of UV and formalin inactivation on the stability and immunogenicity of a Coxsackievirus B1 vaccine. Vaccine *37*, 5962–5971. https://doi.org/10.1016/j.vaccine.2019.08.037.

70. Wang, C.-H., Tschen, S.-Y., and Flehmig, B. (1995). Antigenicity of hepatitis A virus after ultra-violet inactivation. Vaccine *13*, 835–840. https://doi.org/10.1016/0264-410x(94)00054-q.

71. Beck, S.E., Rodriguez, R.A., Hawkins, M.A., Hargy, T.M., Larason, T.C., and Linden, K.G. (2015). Comparison of UV-induced inactivation and RNA damage in MS2 phage across the germicidal UV spectrum. Appl. Environ. Microbiol. *82*, 1468–1474. https://doi.org/10.1128/aem.02773-15.

72. Fazakerley, J.K., Southern, P., Bloom, F., and Buchmeier, M.J. (1991). High resolution in situ hybridization to determine the cellular distribution of lymphocytic choriomeningitis virus RNA in the tissues of persistently infected mice: relevance to arenavirus disease and mechanisms of viral persistence. J. Gen. Virol. *72*, 1611–1625. https://doi.org/10.1099/0022-1317-72-7-1611.

73. Ibraghimov-Beskrovnaya, O., Ervasti, J.M., Leveille, C.J., Slaughter, C.A., Sernett, S.W., and Campbell, K.P. (1992). Primary structure of dystrophin-associated glycoproteins linking dystrophin to the extracellular matrix. Nature *355*, 696–702. https://doi.org/10.1038/355696a0.

74. Campbell, K.P., and Kahl, S.D. (1989). Association of dystrophin and an integral membrane glycoprotein. Nature *338*, 259–262. https://doi.org/10.1038/338259a0.

75. Pipperger, L., Riepler, L., Kimpel, J., Siller, A., Stoitzner, P., Bánki, Z., and von Laer, D. (2021). Differential infection of murine and human dendritic cell subsets by oncolytic vesicular stomatitis virus variants. OncoImmunology *10*, 1959140. https://doi.org/10.1080/2162402x.2021.1959140.

76. Shi, B., Keough, E., Matter, A., Leander, K., Young, S., Carlini, E., Sachs, A.B., Tao, W., Abrams, M., Howell, B., and Sepp-Lorenzino, L. (2011). Biodistribution of small interfering RNA at the organ and cellular levels after lipid nanoparticle-mediated delivery. J. Histochem. Cytochem. *59*, 727–740. https://doi.org/10.1369/0022155411410885.

77. Li, S.-D., and Huang, L. (2008). Pharmacokinetics and biodistribution of nanoparticles. Mol. Pharm. *5*, 496–504. https://doi.org/10.1021/mp800049w.

78. Rattan, R., Bhattacharjee, S., Zong, H., Swain, C., Siddiqui, M.A., Visovatti, S.H., Kanthi, Y., Desai, S., Pinsky, D.J., and Goonewardena, S.N. (2017). Nanoparticle-macrophage interactions: a balance between clearance and cell-specific targeting. Bioorg. Med. Chem. *25*, 4487–4496. https://doi.org/10.1016/j.bmc.2017.06.040.

79. Lang, K.S., and Lang, P.A. (2015). Balancing viral replication in spleen and liver determines the outcome of systemic virus infection. Z. Gastroenterol. *53*, 1432–1435. https://doi.org/10.1055/s-0041-109631.

80. Lang, P.A., Recher, M., Honke, N., Scheu, S., Borkens, S., Gailus, N., Krings, C., Meryk, A., Kulawik, A., Cervantes-Barragan, L., et al. (2010). Tissue macrophages suppress viral replication and prevent severe immunopathology in an interferon-I-dependent manner in mice. Hepatology *52*, 25–32. https://doi.org/10.1002/hep.23640.

81. Seiler, P., Aichele, P., Odermatt, B., Hengartner, H., Zinkernagel, R.M., and Schwendener, R.A. (1997). Crucial role of marginal zone macrophages and marginal zone metallophils in the clearance of lymphocytic choriomeningitis virus infection. Eur. J. Immunol. *27*, 2626–2633. https://doi.org/10.1002/eji.1830271023.

82. Oehen, S., Odermatt, B., Karrer, U., Hengartner, H., Zinkernagel, R., and López-Macías, C. (2002). Marginal zone macrophages and immune responses against viruses. J. Immunol. *169*, 1453–1458. https://doi.org/10.4049/jimmunol.169.3.1453.

83. Ali, S., Mann-Nüttel, R., Schulze, A., Richter, L., Alferink, J., and Scheu, S. (2019). Sources of type I interferons in infectious immunity: plasmacytoid dendritic cells not always in the driver's seat. Front. Immunol. *10*, 778. https://doi.org/10.3389/fimmu.2019.00778.

84. Shaabani, N., Duhan, V., Khairnar, V., Gassa, A., Ferrer-Tur, R., Häussinger, D., Recher, M., Zelinskyy, G., Liu, J., Dittmer, U., et al. (2016). CD169+ macrophages regulate PD-L1 expression via type I interferon and thereby prevent severe immunopathology after LCMV infection. Cell Death Dis. *7*, e2446. https://doi.org/10.1038/cddis.2016.350.

85. Ferguson, M.S., Lemoine, N.R., and Wang, Y. (2012). Systemic delivery of oncolytic viruses: hopes and hurdles. Adv. Virol. *2012*, 805629. https://doi.org/10.1155/2012/805629.

86. Valic, M.S., and Zheng, G. (2019). Research tools for extrapolating the disposition and pharmacokinetics of nanomaterials from preclinical animals to humans. Theranostics *9*, 3365–3387. https://doi.org/10.7150/thno.34509.

87. Muik, A., Kneiske, I., Werbizki, M., Wilflingseder, D., Giroglou, T., Ebert, O., Kraft, A., Dietrich, U., Zimmer, G., Momma, S., and von Laer, D. (2011). Pseudotyping vesicular stomatitis virus with lymphocytic choriomeningitis virus glycoproteins enhances infectivity for glioma cells and minimizes neurotropism. J. Virol. *85*, 5679–5684. https://doi.org/10.1128/jvi.02511-10.

88. Muik, A., Stubbert, L.J., Jahedi, R.Z., Geiß, Y., Kimpel, J., Dold, C., Tober, R., Volk, A., Klein, S., Dietrich, U., et al. (2014). Re-engineering vesicular stomatitis virus to abrogate neurotoxicity, circumvent humoral immunity, and enhance oncolytic potency. Cancer Res. *74*, 3567–3578. https://doi.org/10.1158/0008-5472.can-13-3306.

89. Livak, K.J., and Schmittgen, T.D. (2001). Analysis of relative gene expression data using real-time quantitative PCR and the 2−ΔΔC T method. Methods *25*, 402–408. https://doi.org/10.1006/meth.2001.1262.

90. Hamilton, M.A., Russo, R.C., and Thurston, R.V. (1977). Trimmed Spearman-Karber method for estimating median lethal concentrations in toxicity bioassays. Environ. Sci. Technol. *11*, 714–719. https://doi.org/10.1021/es60130a004.